This is the accepted version of the following article: Eduard Chemyakin, Sharon Burton, Alexei Kolgotin, Detlef Muller, Chris Hostetler, and Richard Ferrare, 'Retrieval of aerosol parameters from multiwavelength lidar: investigation of the underlying inverse mathematical problem', *Applied Optics* Vol 55(9): 2188-2202 (2016). The final, published version is available online via doi: https://doi.org/10.1354/AO.55.002188

Retrieval of aerosol parameters from multiwavelength lidar. Investigation of underlying inverse mathematical problem.

Eduard Chemyakin,[1,*] Sharon Burton,[2] Alexei Kolgotin,[3] Detlef Müller,[4,1] Chris Hostetler,[2] and Richard Ferrare[2]

[1] *Science Systems and Applications, Inc., NASA Langley Research Center, Mail Stop 475, Hampton, VA 23681-2199, USA*

[2] *NASA Langley Research Center, Mail Stop 401A, Hampton, VA 23681-2199, USA*

[3] *Physics Instrumentation Center, A. M. Prokhorov General Physics Institute, Troitsk, Moscow Region, 142190, Russia*

[4] *University of Hertfordshire, College Lane, Hatfield, AL10 9AB Hertfordshire, United Kingdom*

[*] *Corresponding author: eduard.chemyakin@ssaihq.com*

Compiled February 11, 2016

We present an investigation of some important mathematical and numerical features related to the retrieval of microphysical parameters (complex refractive index, single-scattering albedo, effective radius, total number, surface area, and volume concentrations) of ambient aerosol particles using multiwavelength Raman or high-spectral-resolution lidar. Using simple examples we prove the non-uniqueness of an inverse solution to be the major source of the retrieval difficulties. Some theoretically possible ways of partially compensating for these difficulties are offered. For instance, an increase in the variety of input data via combination of lidar and certain passive remote sensing instruments will be helpful to reduce the error of estimation of complex refractive index. Also we demonstrate significant interference between Aitken and accumulation aerosol modes in our inversion algorithm and confirm that the solutions can be better constrained by limiting the particle radii. Applying a combination of analytical approach and numerical simulations, we explain statistical behavior of the microphysical size parameters. We reveal and clarify why the total surface area concentration is consistent even in the presence of non-unique solution sets and is on average the most stable parameter to be estimated, as long as at least one extinction optical coefficient is employed. We find that for a selected particle size distributions the total surface area and volume concentrations can be quickly retrieved with fair precision using only a single extinction coefficients in a simple arithmetical relationship.

OCIS codes: 000.3860, 010.1100, 010.1110, 010.3640, 280.0280.

1. Introduction

Aerosols are fairly minor constituents of the Earth's atmosphere, but they are able to affect its radiative energy balance and thus participate in shaping of the Earth's environment [1]. Various types of atmospheric particles differently influence regional and global climate through direct and indirect radiative effects. They are not well understood yet because of a multitude of connection factors and feedback mechanisms. Aerosols are considered to be the dominant uncertainty in assessing anthropogenic forcing of climate change [1]. Regular monitoring over long temporal and global spatial scales is needed to address the gaps in knowledge of the role of microphysical and optical properties of aerosols in these complicated processes.

Light identification, detection, and ranging

(lidar) remote sensing instruments have all the potential to play a crucial role in atmospheric research as they uniquely provide information about ambient aerosols properties on a comparably high vertical resolution. A significant leap in technology development has recently been achieved by NASA Langley Research Centers (LaRC) airborne "3 backscatter (β) + 2 extinction (α)" High-Spectral-Resolution Lidar (HSRL-2). This instrument participated in several successful field campaigns, and some of the results already have been published [2]. An article summarizing more results is in preparation [3].

Climate study applications require knowledge of the parameters that can't be directly measured by lidar, but some of them can be retrieved by specialized algorithms using lidar data. These algorithms solve mathematical problems that have multiple theoretical and numerical features. They need to be discovered, analyzed and carefully considered in order to provide the climate research community with trustworthy retrieval products.

Simplifying the classical definition [4], a mathematical problem is called well posed if the solution of that problem (i) exists, (ii) is unique, and (iii) is stable. The term uniqueness is used to indicate that exactly one object with a certain property exists. The term stability reflects the ability to result in small variations of solution under small perturbations of initial conditions. A problem is ill-posed if (i), (ii) or (iii) fail [4].

The topic of estimation of aerosol parameters from multiwavelength lidar was actively developed in the recent two decades. Several algorithms were proposed and tested by research groups from different institutions. The list of algorithms includes but is not limited to an adapted form of the principal component analysis [5, 6], inversion with Tikhonov's regularization [7–11], the hybrid regularization method [12, 13], the linear estimation approach [14], and the arrange and average algorithm [15]. Currently, there is no published study revealing the whole picture of the retrievals complexity and multifacetedness. Reading the topic related literature [5–15], we did not find satisfactory answers to many of our questions. Some of them previously were not explained in terms of equations or numerical demonstrations. For instance, what makes the retrieval system ill-posed, or why there is a certain stable pattern in the quality of microphysical products? The purpose of this paper is to continue with our study that filling the gap with explanations and supporting examples on these and other questions [16]. Our ultimate goal is to help ourselves and others to improve the quality of estimations through better understanding of the inversion background.

In Section 2 we reveal the major problem and describe the analysis technique which includes investigations using the look-up table. In Section 3 we explore the interference between the Aitken and accumulation mode particle retrievals. In Section 4 we present our explanation of the statistical behavior of the microphysical size parameters. Section 5 provides more insight on the details of Section 4 through the analysis of extinction number kernel functions. Section 6 summarizes our findings.

2. Non-Uniqueness of the Solution

A. *Statement of Mathematical Problem*

The optical coefficients of aerosols can be calculated according to the following equation:

$$l_\lambda = \int_0^\infty K_l\left(m, r, \lambda, p\right) f\left(r\right) \mathrm{d}r. \qquad (1)$$

The term l_λ describes the optical data at measurement wavelength λ for one altitude- and time-resolved acquisition point. The symbol l denotes the type of optical data (β – backscatter, α – extinction, and ς – scattering). The function $f\left(r\right)$ describes the particle size distribution (PSD) expressed as the number of particles per unit volume between particle radius r and $r+\mathrm{d}r$. The terms $K_\beta\left(m, r, \lambda, p\right)$, $K_\alpha\left(m, r, \lambda, p\right)$, and $K_\varsigma\left(m, r, \lambda, p\right)$ describe, respectively, the backscatter, extinction, and scattering number kernel functions.

The kernel functions $K_l\left(m, r, \lambda, p\right)$ depend on the complex refractive index (CRI), i. e., $m = m_\mathrm{R} - i \cdot m_\mathrm{I}$ that describes the material composition of the particles, on the radius r of

the particles, as well as on their shape properties p. The expression m_{R} denotes the real part, and the expression m_{I} describes the imaginary part of the CRI. In this study we consider only spherical aerosols, which allows us to apply the Mie-scattering theory in computations of the particle optical properties [17]. For easier reading, the reference to the shape property p will therefore be omitted.

The set of several different optical coefficients $\{l_\lambda\}$ is assumed to be known as the result of the real measurements or numerical simulations. The unknown parameters to be retrieved out of the Eq. (1) are the real (m_{R}) and imaginary (m_{I}) parts of the CRI, and the PSD $f(r)$. Estimating these after solving the inverse problem, one can get access to a huge variety of microphysical parameters. The most popular and useful parameters in the atmospheric research applications are the total number concentration:

$$n_{\mathrm{t}} = \int_0^\infty f(r)\,\mathrm{d}r, \tag{2}$$

the total surface area concentration:

$$s_{\mathrm{t}} = 4\pi \int_0^\infty r^2 f(r)\,\mathrm{d}r, \tag{3}$$

the total volume concentration:

$$v_{\mathrm{t}} = \frac{4\pi}{3} \int_0^\infty r^3 f(r)\,\mathrm{d}r, \tag{4}$$

the effective radius:

$$r_{\mathrm{eff}} = \frac{3v_{\mathrm{t}}}{s_{\mathrm{t}}} = \frac{\int_0^\infty r^3 f(r)\,\mathrm{d}r}{\int_0^\infty r^2 f(r)\,\mathrm{d}r}, \tag{5}$$

the single-scattering albedo:

$$\omega_\lambda = \frac{\varsigma_\lambda}{\alpha_\lambda} = \frac{\int_0^\infty K_\varsigma(m,r,\lambda)\, f(r)\,\mathrm{d}r}{\int_0^\infty K_\alpha(m,r,\lambda)\, f(r)\,\mathrm{d}r}, \tag{6}$$

and so on. This very short list can be extended further, but in this study we only pay attention to these few microphysical parameters.

B. Simple Examples of Failure of Uniqueness

Let us consider the numerical simulation of the advanced "$3\beta + 2\alpha$" configuration of the multiwavelength Raman/high-spectral-resolution lidar. In this case the set $\{\beta_{355}, \beta_{532}, \beta_{1064}, \alpha_{355}, \alpha_{532}\}$ consisting of the backscatter coefficients at 355, 532, and 1064 nm, and extinction coefficients at 355 and 532 nm is available as input information.

We will use the logarithmic-normal distribution of the form:

$$f(r) = \frac{n_0}{r\sqrt{2\pi}\ln\sigma} \exp\left[-\frac{\left(\ln r - \ln r_{\mathrm{med}}\right)^2}{2\ln^2\sigma}\right] \tag{7}$$

as the PSD $f(r)$ in Eq. (1).

The parameter r_{med} describes the count median radius with respect to the number concentration distribution. The count median radius is defined as the radius above which there are as many particles as there are particles with radii below r_{med}. The term σ denotes the geometric standard deviation whereas $\ln\sigma$ is commonly referred to as the mode width. The parameter n_0 with the positive range of possible values is responsible for the linear variation of the total number concentration [see Eq. (2)]. The values of optical coefficients of the aerosols [see Eq. (1)], their total surface area and volume concentrations [see Eqs. (3)–(4)] also would change proportionally to n_0.

Equation (7) describes a monomodal PSD. We use this logarithmic-normal shape as it is a reasonable approximation for the shape of naturally occurring PSDs [18, 19].

For the first look, the considered inversion problem has a good chance to be well-posed. There are five measured quantities $\{\beta_{355}, \beta_{532}, \beta_{1064}, \alpha_{355}, \alpha_{532}\}$ and five values to be retrieved, i. e., $\{n_0, r_{\mathrm{med}}, \sigma, m_{\mathrm{R}}, m_{\mathrm{I}}\}$. The number of unknowns is exactly equal to the number of measurements.

Let us calculate the reference "$3\beta + 2\alpha$" optical coefficients using Eq. (1) with the geometrical parameters of PSD $n_0^{\mathrm{ref.A}} = 1\ \mathrm{cm}^{-3}$, $r_{\mathrm{med}}^{\mathrm{ref.A}} = 0.02\ \mu\mathrm{m}$, $\sigma^{\mathrm{ref.A}} = 2.5$, and the CRI with real part $m_{\mathrm{R}}^{\mathrm{ref.A}} = 1.5$ and imaginary part $m_{\mathrm{I}}^{\mathrm{ref.A}} = 0.015$ [see Table 1, column "Reference A"]. The CRI was kept independent of particle size and wavelength. The lower and upper integration limits in Eq. (1) were set from 0.001 to 50 μm. The radius stepsize in the computations was 0.001 μm. Two optional "$3\beta + 2\alpha$" optical data sets were simulated using alternative input

parameters [see Table 1, columns "Option A.1" and "Option A.2"]. These parameters were intentionally chosen in a way that the optical data later are reproduced with high similarity to the reference data.

The existence of the solution of the inverse problem expressed as the Eq. (1) is obvious for this numerically simulated example. Therefore, the first of the three conditions for well-posed problems is fulfilled. However, Table 1 clearly demonstrates the non-uniqueness of the mathematical solution of the microphysical parameters retrievals. We provided three different sets of inputs that resulted in almost exactly the same "$3\beta + 2\alpha$" optical coefficients. One can see that the relative difference between the corresponding reference and optional optical data is less than 0.1% [see Table 1]. We consider this to be sufficient to confirmation the ill-posedness of the inverse problem at least in some cases because the condition (ii) is not fulfilled. An error of 0.1% is much smaller than the measurement error that can be achieved by any Raman or high-spectral-resolution lidar. We can barely expect to have optical data with better quality in terms of noise, but in this case it is not even necessary to introduce any noise. The precisely defined "$3\beta+2\alpha$" optical coefficients are well reproduced in multiple ways by just using different input parameters.

One might have the impression that the considered "Reference A" geometrical input parameters are extreme because the low count median radius ($r_{\mathrm{med}}^{\mathrm{ref.A}} = 0.02$ μm) even in combination with high geometric standard deviation ($\sigma^{\mathrm{ref.A}} = 2.5$) results in a very narrow PSD. The absolute majority of the particles have a radius below 100 nm [see Fig. 1, solid bell shaped curve of "A" series]. This barely realistic showcase was selected because it obviously reveals the complexity of the underlying inverse problem due to the effective radius ($r_{\mathrm{eff.A}} = 0.163156$ μm) fitting exactly into the accumulation mode range of real retrievals.

Figure 1 shows all of the "$3\beta+2\alpha$" backscatter and extinction number kernel functions together with the monomodal logarithmic-normal PSDs that are used in this example. The backscatter kernels at the same wavelength look very similar for the reference and both optional cases up to a particle radius of about 100 nm. A noticeable oscillation that is helping us to distinguish them begins only after that border [see Fig. 1, three top blocks]. The extinction kernels are more easily distinguishable from each other [see Fig. 1, bottom two blocks]. Despite this, the integration in Eq. (1) results in quantities that are different less than 0.1% between themselves [see Table 1, lines $\Delta\alpha_{355}$ and $\Delta\alpha_{532}$].

From the absorption point of view, the "Reference A" column represents moderately absorbing aerosols ($m_{\mathrm{I}}^{\mathrm{ref.A}} = 0.015$). The "Option A.1" is a low absorbing ($m_{\mathrm{I}}^{(A.1)} \approx 0.0025$) and the "Option A.2" is a highly absorbing ($m_{\mathrm{I}}^{(A.2)} \approx 0.0405$) mixture of ambient particles [see Table 1]. The purpose of this example is to demonstrate the theoretical possibility of having the distribution of spherical particles with radically different absorbing properties and very similar quantitative interactions with incident laser radiation at certain wavelengths.

In our studies we are highly interested in the accumulation mode of aerosols. These are the particles with radii between 50 nm and 1.25 μm, and a lifetime in the atmosphere of days to weeks [18, 19]. The aerosols with radii below 50 nm belong to the Aitken and nucleation modes. Their lifetime is estimated to be only a few hours with further coagulation with larger particles [18, 19].

The first example represents the Aitken mode particles [see Table 1]. The accumulation mode aerosols are considered in our second example [see Table 2]. It demonstrates the input parameters that again result in almost identical "$3\beta + 2\alpha$" optical coefficients for the reference and two optional cases. We kept the same reference CRI but shifted the PSD to cover bigger particles sizes [see Fig. 1, solid bell shaped curve of "B" series]. The true effective radius is more than twice as large compared to the first example [see Tables 1–2, "Reference" columns].

These two examples are showing that the non-uniqueness of the inverse solution is common for the mathematical problem to be solved. The am-

bient particles of different size modes are equally affected. We also noticed that it is much easier to find an alternate solution with higher imaginary parts than the reference one has. This is consistent with the outcome of our previous studies, which generally showed an overestimation of the imaginary part as a result of microphysical parameters retrievals [7–11, 15, 16].

C. Look-Up Table

Let us move away from analyzing solutions-pairs one by one to a more statistical approach with the look-up table (LUT). That LUT contains particle backscatter, extinction, and scattering coefficients at 355, 532, and 1064 nm, CRI, effective radius, total surface area, and volume concentrations. The optical parameters are calculated with a Mie scattering code appropriate for spherical particles [17]. The input parameters for the computations are PSD and CRI. The normalized PSDs are chosen in a way that the total number concentration n_t [see Eq. (2)] is equal to 1 cm^{-3}, which is the case if $n_0 = 1\ \mathrm{cm}^{-3}$. The range of PSDs and CRIs in the LUT is sufficiently broad to cover realistic values for atmospheric aerosols [20].

Table 3 lists the parameters of the normalized monomodal logarithmic-normal PSDs and CRIs that were used in generating the LUT. We used 42 different values of real parts and 52 imaginary parts of the CRI. The PSDs are given in terms of the total surface area concentration and effective radius. This is done in order to have the controllable distribution of these two microphysical parameters. The total surface area concentration varies from 0.005 to approximately 6.36 $\frac{\mu\mathrm{m}^2}{\mathrm{cm}^3}$. For the constant total number concentration, 362 values are considered. The effective radius is varying from 0.025 to approximately 2.57 μm, and 235 values are considered. The next value is 2% larger than the previous one for both parameters. For instance, the starting value for the effective radius is 0.025 μm. The next ones are $0.025 \cdot 1.02 = 0.0255$ μm, $0.0255 \cdot 1.02 = 0.02601$ μm, and so on.

Theoretically, the designed LUT should contain $42 \cdot 52 \cdot 362 \cdot 235 = 185,792,880$ entries. Practically, the number of the LUT elements is equal to 122,675,280. The constraining limitation that reduces the number of entries so significantly is mathematically explained below. The physical meaning of this constraint is that the low values of effective radius and the high values of total surface area concentration can't be simultaneously reproduced using a normalized monomodal logarithmic-normal PSD.

The connection between the total surface area concentration s_t and effective radius r_eff on the one side, and the count median radius r_med and geometric standard deviation σ on the other in our particular case can be obtained analytically. First, we have to substitute the logarithmic-normal PSD $f(r)$ formerly described by Eq. (7) into Eqs. (3) and (5). Then, the application of direct integration will allow us to express these two chosen microphysical parameters via n_0, r_med, and σ as:

$$s_\mathrm{t} = 4\pi n_0 r_\mathrm{med}^2 \exp\left(2\ln^2\sigma\right), \tag{8}$$

$$r_\mathrm{eff} = r_\mathrm{med} \exp\left(2.5\ln^2\sigma\right). \tag{9}$$

For the purpose of error analysis in Section 4, we will need the analytical form for the total number and volume concentrations. These two parameters can be presented as:

$$n_\mathrm{t} = n_0, \tag{10}$$

$$v_\mathrm{t} = \frac{4\pi}{3} n_0 r_\mathrm{med}^3 \exp\left(4.5\ln^2\sigma\right). \tag{11}$$

In a general case, the direct integration with monomodal logarithmic-normal PSD $f(r)$ that is described by its variables n_0, r_med, and σ will result in:

$$\int_0^\infty r^\mathrm{k} f(r)\,\mathrm{d}r = n_0 r_\mathrm{med}^\mathrm{k} \exp\left(\frac{\mathrm{k}^2}{2}\ln^2\sigma\right). \tag{12}$$

In the opposite direction, the expression of the r_med and σ via the s_t and r_eff from Eqs. (8) and (9) will give us:

$$r_\mathrm{med} = r_\mathrm{eff} \exp\left(\frac{5}{6}\ln\frac{s_\mathrm{t}}{4\pi n_0 r_\mathrm{eff}^2}\right), \tag{13}$$

$$\sigma = \exp\sqrt{-\frac{1}{3}\ln\frac{s_{\rm t}}{4\pi n_0 r_{\rm eff}^2}}. \qquad (14)$$

According to Eq. (14), the geometric standard deviation σ can only be computed in real numbers if the value under the square root is non-negative. That is the case if:

$$\frac{s_{\rm t}}{4\pi r_{\rm eff}^2} < n_0 = 1\ {\rm cm}^{-3}. \qquad (15)$$

This limitation reduces the number of PSDs in the LUT from $362 \cdot 235 = 85,070$ to 56,170. The spatial distribution of the remaining combinations of the total surface area concentration and effective radius is shown in Fig. 2. As predicted by Eq. (15), on the bottom side of the plot one can see the parabolic shape gap in the coverage of the LUT parameters.

D. Example of Non-Uniqueness as Major Issue in the "$3\beta + 2\alpha$" Retrievals

The parameter ranges covered by the LUT were chosen to present the range of parameters found in ambient aerosols. For further analysis, let us select the situations that are similar to the "Reference A" case which is described by the set of its "$3\beta + 2\alpha$" optical coefficients $\{\beta_{355}^{\rm ref.A}, \beta_{532}^{\rm ref.A}, \beta_{1064}^{\rm ref.A}, \alpha_{355}^{\rm ref.A}, \alpha_{532}^{\rm ref.A}\}$ [see Table 1]. We consider the entry number j of the LUT represented by its optical data $\left\{\beta_{355}^{j}, \beta_{532}^{j}, \beta_{1064}^{j}, \alpha_{355}^{j}, \alpha_{532}^{j}\right\}$ to be similar to the "Reference A" case within the manually set threshold δ, if the coefficient $n_{3\beta+2\alpha}^{j}$ can be found that makes the normalized discrepancy $\rho_{3\beta+2\alpha}^{j}$ to be less than δ, i. e.,

$$\rho_{3\beta+2\alpha}^{j} = \frac{1}{5}\left(\left|\frac{\beta_{355}^{\rm ref.A} - n_{3\beta+2\alpha}^{j}\beta_{355}^{j}}{\beta_{355}^{\rm ref.A}}\right| + \left|\frac{\beta_{532}^{\rm ref.A} - n_{3\beta+2\alpha}^{j}\beta_{532}^{j}}{\beta_{532}^{\rm ref.A}}\right| + \left|\frac{\beta_{1064}^{\rm ref.A} - n_{3\beta+2\alpha}^{j}\beta_{1064}^{j}}{\beta_{1064}^{\rm ref.A}}\right| + \left|\frac{\alpha_{355}^{\rm ref.A} - n_{3\beta+2\alpha}^{j}\alpha_{355}^{j}}{\alpha_{355}^{\rm ref.A}}\right| + \left|\frac{\alpha_{532}^{\rm ref.A} - n_{3\beta+2\alpha}^{j}\alpha_{532}^{j}}{\alpha_{532}^{\rm ref.A}}\right|\right) \cdot 100\% < \delta\%. \qquad (16)$$

The simplest way to estimate the unitless coefficient $n_{3\beta+2\alpha}^{j}$ is:

$$n_{3\beta+2\alpha}^{j} = \frac{1}{5}\left(\frac{\beta_{355}^{\rm ref.A}}{\beta_{355}^{j}} + \frac{\beta_{532}^{\rm ref.A}}{\beta_{532}^{j}} + \frac{\beta_{1064}^{\rm ref.A}}{\beta_{1064}^{j}} + \frac{\alpha_{355}^{\rm ref.A}}{\alpha_{355}^{j}} + \frac{\alpha_{532}^{\rm ref.A}}{\alpha_{532}^{j}}\right). \qquad (17)$$

Using Eq. (16), we are testing all of the $j = 1 \ldots 122,675,280$ entries of the LUT. The subset $\left\{{\rm LUT}_{3\beta+2\alpha}^{\delta}\right\}$ consists of the LUT elements that passed through that test, i. e., with a discrepancy $\rho_{3\beta+2\alpha}^{j_1}$ smaller than the manually chosen threshold δ. This subset can be analyzed from different perspectives. We are interested in the distribution of CRIs, as well as the behavior of microphysical size parameters within this distribution, because the subset content is likely to be used for the final solution averaging in one of our inversion algorithms [7–11, 15]. The unitless coefficients $n_{3\beta+2\alpha}^{j_1}$ can be treated as the total number concentrations because numerically they are equal in the case of used LUT and "Reference A" optical data set. The imaginary part of the CRI deserves special attention because it is the most critical parameters for the estimation of the single-scattering albedo that describes the absorbing properties of aerosols [see Eq. (6)].

The total surface area ($s_{\rm t}^{j_1}$) and volume ($v_{\rm t}^{j_1}$) concentrations in the subset $\left\{{\rm LUT}_{3\beta+2\alpha}^{\delta}\right\}$ have to be scaled up by the coefficient $n_{3\beta+2\alpha}^{j_1}$ before carrying out the analysis as:

$$\hat{s}_{\rm t}^{j_1} = n_{3\beta+2\alpha}^{j_1} s_{\rm t}^{j_1} \quad \text{and} \quad \hat{v}_{\rm t}^{j_1} = n_{3\beta+2\alpha}^{j_1} v_{\rm t}^{j_1}, \qquad (18)$$

where $\hat{s}_{\rm t}^{j_1}$ and $\hat{v}_{\rm t}^{j_1}$ are the corrected values. The index j_1 runs from 1 to the number of entries in the subset $\left\{{\rm LUT}_{3\beta+2\alpha}^{\delta}\right\}$.

Figure 3 demonstrates in a qualitative manner the behavior of microphysical size parameters targeted in this study; one block per parameter. The normalized discrepancy threshold δ in this test was selected to be 0.3%, which is sufficient to provide the representative sample. The center of each bubble is located in the coordinates given by the real (horizontal axis) and imaginary (vertical axis) parts of the CRIs of the $\left\{{\rm LUT}_{3\beta+2\alpha}^{0.3\%}\right\}$ subset entries. The radius of each bubble shows the value of the corresponding size parameter. The true "Reference A" value of the microphysical size parameter is shown in the right bottom corner of each block. One can see that the trace of "3β+2α" optical data sets similar within 0.3% to the set $\{\beta_{355}^{\rm ref.A}, \beta_{532}^{\rm ref.A}, \beta_{1064}^{\rm ref.A}, \alpha_{355}^{\rm ref.A}, \alpha_{532}^{\rm ref.A}\}$ is quite narrow and stretches from the minimum to maximum values of the imaginary part. In Table 1 we provide an example of three different combinations of the CRIs and PSDs that

are reproducing almost the same "$3\beta + 2\alpha$" optical coefficients. Figure 3 shows that there are more than two options to do so and this is the main reason why the retrieval of the imaginary part can be such a complicated task in general case [5–15]. We would like to point out that the displayed situation is not unique. In our numerical simulations we often see similar output. The results for effective radius and total volume concentration look qualitatively analogous, i. e., in this particular example their overall estimations are getting higher for lower imaginary parts [see Fig. 3, top left and bottom right blocks]. The total surface area concentration has about the same range of retrieved values for the whole diapason of imaginary parts [see Fig. 3, bottom left block]. In Sections 4 and 5 we will pay special attention to this impressive consistency and make it serve for some useful conclusions. The total number concentration, which is presented here by the unitless coefficient $n_{3\beta+2\alpha}$, is the most unpredictable among the four considered microphysical size parameters [see Fig. 3, top right block]. It has the largest ratio of the biggest to the smallest parameter value at the same CRI point.

For the demonstration of key mathematical features in this study, we use monomodal PSDs. In the real atmosphere, PSDs are commonly believed to be at least bimodal or multimodal [18, 19]. We expect that if we expand our LUT to include bimodal PSDs similar to ambient aerosol distributions, then the non-uniqueness of the inverse solution will become even more pronounced.

E. Effect of Alternate Instrument Configurations on Non-Uniqueness

Before moving further, let us consider four alternative instrument configurations and provide a quick estimation of the CRI distribution within the corresponding LUT subsets. We will test the "3β", "$2\beta + 1\alpha$", and "$3\beta + 1\alpha$" lidar configurations as we did for our arrange and average algorithm [15], plus the "$2\beta + 1\alpha + 1\varsigma$" one as a theoretically possible combination of active and passive remote sensors.

The "3β" configuration is the extreme scenario as it only uses particle backscatter coefficients at 355, 532, and 1064 nm. The "$2\beta+1\alpha$" lidar configuration consists of backscatter coefficients at 532 and 1064 nm, and the extinction coefficient at 532 nm. This configuration reflects the first generation of airborne High-Spectral-Resolution Lidar (HSRL-1) built at NASA LaRC [21]. The HSRL-1 instrument collected a huge amount of "$2\beta + 1\alpha$" data during its numerous field campaigns. The "$3\beta+1\alpha$" configuration consists of backscatter coefficients at 355, 532, and 1064 nm, and the extinction coefficient at 355 nm. This configuration is interesting from the perspective of the ground-based Raman lidar community because the nitrogen Raman signal is considerably stronger at 355 nm compared to 532 nm. It allows us to measure the extinction coefficient with higher precision at 355 nm. The "$2\beta + 1\alpha + 1\varsigma$" configuration has similar to "$2\beta + 1\alpha$" wavelengths for the backscatter and extinction coefficients, and uses a scattering coefficient at 532 nm. Instead of scattering, the absorption optical coefficient or single-scattering albedo can be used. This configuration is purely theoretical at the moment and represents the combination of lidar and some passive remote sensing instruments.

For these four instrumental configurations we need to define the normalized discrepancies as:

$$\rho^j_{3\beta} = \frac{1}{3}\left(\left|\frac{\beta^{\text{ref.A}}_{355} - n^j_{3\beta}\beta^j_{355}}{\beta^{\text{ref.A}}_{355}}\right| + \left|\frac{\beta^{\text{ref.A}}_{532} - n^j_{3\beta}\beta^j_{532}}{\beta^{\text{ref.A}}_{532}}\right| + \left|\frac{\beta^{\text{ref.A}}_{1064} - n^j_{3\beta}\beta^j_{1064}}{\beta^{\text{ref.A}}_{1064}}\right|\right)\cdot 100\%, \quad (19)$$

$$\rho^j_{2\beta+1\alpha} = \frac{1}{3}\left(\left|\frac{\beta^{\text{ref.A}}_{532} - n^j_{2\beta+1\alpha}\beta^j_{532}}{\beta^{\text{ref.A}}_{532}}\right| + \left|\frac{\beta^{\text{ref.A}}_{1064} - n^j_{2\beta+1\alpha}\beta^j_{1064}}{\beta^{\text{ref.A}}_{1064}}\right| + \left|\frac{\alpha^{\text{ref.A}}_{532} - n^j_{2\beta+1\alpha}\alpha^j_{532}}{\alpha^{\text{ref.A}}_{532}}\right|\right)\cdot 100\%, \quad (20)$$

$$\rho^j_{3\beta+1\alpha} = \frac{1}{4}\left(\left|\frac{\beta^{\text{ref.A}}_{355} - n^j_{3\beta+1\alpha}\beta^j_{355}}{\beta^{\text{ref.A}}_{355}}\right| + \left|\frac{\beta^{\text{ref.A}}_{532} - n^j_{3\beta+1\alpha}\beta^j_{532}}{\beta^{\text{ref.A}}_{532}}\right| + \left|\frac{\beta^{\text{ref.A}}_{1064} - n^j_{3\beta+1\alpha}\beta^j_{1064}}{\beta^{\text{ref.A}}_{1064}}\right| + \left|\frac{\alpha^{\text{ref.A}}_{355} - n^j_{3\beta+1\alpha}\alpha^j_{355}}{\alpha^{\text{ref.A}}_{355}}\right|\right)\cdot 100\%, \quad (21)$$

$$\rho^j_{2\beta+1\alpha+1\varsigma} = \frac{1}{4}\left(\left|\frac{\beta^{\text{ref.A}}_{532} - n^j_{2\beta+1\alpha+1\varsigma}\beta^j_{532}}{\beta^{\text{ref.A}}_{532}}\right| + \left|\frac{\beta^{\text{ref.A}}_{1064} - n^j_{2\beta+1\alpha+1\varsigma}\beta^j_{1064}}{\beta^{\text{ref.A}}_{1064}}\right| + \left|\frac{\alpha^{\text{ref.A}}_{532} - n^j_{2\beta+1\alpha+1\varsigma}\alpha^j_{532}}{\alpha^{\text{ref.A}}_{532}}\right| + \left|\frac{\varsigma^{\text{ref.A}}_{532} - n^j_{2\beta+1\alpha+1\varsigma}\varsigma^j_{532}}{\varsigma^{\text{ref.A}}_{532}}\right|\right)\cdot 100\%, \quad (22)$$

and the corresponding unitless coefficients:

$$n^j_{3\beta} = \frac{1}{3}\left(\frac{\beta^{\text{ref.A}}_{355}}{\beta^j_{355}} + \frac{\beta^{\text{ref.A}}_{532}}{\beta^j_{532}} + \frac{\beta^{\text{ref.A}}_{1064}}{\beta^j_{1064}}\right), \quad (23)$$

$$n^j_{2\beta+1\alpha} = \frac{1}{3}\left(\frac{\beta^{\text{ref.A}}_{532}}{\beta^j_{532}} + \frac{\beta^{\text{ref.A}}_{1064}}{\beta^j_{1064}} + \frac{\alpha^{\text{ref.A}}_{532}}{\alpha^j_{532}}\right), \quad (24)$$

$$n^j_{3\beta+1\alpha} = \frac{1}{4}\left(\frac{\beta^{\text{ref.A}}_{355}}{\beta^j_{355}} + \frac{\beta^{\text{ref.A}}_{532}}{\beta^j_{532}} + \frac{\beta^{\text{ref.A}}_{1064}}{\beta^j_{1064}} + \frac{\alpha^{\text{ref.A}}_{355}}{\alpha^j_{355}}\right), \quad (25)$$

$$n^j_{2\beta+1\alpha+1\varsigma} = \frac{1}{4}\left(\frac{\beta^{\text{ref.A}}_{532}}{\beta^j_{532}} + \frac{\beta^{\text{ref.A}}_{1064}}{\beta^j_{1064}} + \frac{\alpha^{\text{ref.A}}_{532}}{\alpha^j_{532}} + \frac{\varsigma^{\text{ref.A}}_{532}}{\varsigma^j_{532}}\right), \quad (26)$$

where the entry number $j = 1 \ldots 122{,}675{,}280$ of the LUT in a general case is represented by its optical data $\left\{\beta^j_{355}, \beta^j_{532}, \beta^j_{1064}, \alpha^j_{355}, \alpha^j_{532}, \varsigma^j_{355}\right\}$ and compared to the "Reference A" extended set of coefficients $\{\beta^{\text{ref.A}}_{355}, \beta^{\text{ref.A}}_{532}, \beta^{\text{ref.A}}_{1064}, \alpha^{\text{ref.A}}_{355}, \alpha^{\text{ref.A}}_{532}, \varsigma^{\text{ref.A}}_{355}\}$ [see Table 1 for the PSD variables and CRI].

The LUT subsets $\left\{\text{LUT}^{0.3\%}_{3\beta}\right\}$, $\left\{\text{LUT}^{0.3\%}_{2\beta+1\alpha}\right\}$, $\left\{\text{LUT}^{0.3\%}_{3\beta+1\alpha}\right\}$, and $\left\{\text{LUT}^{0.3\%}_{2\beta+1\alpha+1\varsigma}\right\}$ consist of the LUT elements whose corresponding normalized discrepancies [see Eqs. (19)–(22)] are less than 0.3%. The distributions of the CRIs for these four subsets are shown in Fig. 4, one block per instrumental configuration.

The "3β" lidar configuration has the broadest trace of its LUT subset on the CRI plane [see Fig. 4, top left block]. This explains the poorest performance of the "3β" configuration in our arrange and average algorithm [15]. The CRI barely has a chance to be estimated with acceptable error in such a situation. The same number of optical data, but employing just one extinction coefficient can significantly reduce the amount of outliers [see Fig. 4, "$2\beta + 1\alpha$" block]. One more backscatter coefficient makes the situation even better [see Fig. 4, "$3\beta + 1\alpha$" block]. These three blocks of Fig. 4 are in good agreement with our earlier results [15]. The best theoretical performance is shown in this example by the "$2\beta + 1\alpha + 1\varsigma$" configuration [see Fig. 4, bottom right block]. The significant reduction of the outliers population in the bottom right block compared to the top right one is obvious [see Fig. 4, "$2\beta + 1\alpha$" block]. The combination of only one precisely measured extinction and scattering (or absorption, or single-scattering albedo) optical coefficients being measured at the same wavelength can significantly improve the uniqueness aspect of the original mathematical problem [see Section 1]. We would like to pay special attention to this conclusion because a smaller number of input optical coefficients (four for "$2\beta + 1\alpha + 1\varsigma$" versus five for "$3\beta + 2\alpha$") results in a competitive quality of retrievals. The trace of the $\left\{\text{LUT}^{0.3\%}_{2\beta+1\alpha+1\varsigma}\right\}$ subset on the CRI plane is much more compact even compared to the $\left\{\text{LUT}^{0.3\%}_{3\beta+2\alpha}\right\}$ [see Figs. 3–4].

Let us expand this valuable result into a wider picture. We have to use more than just one reference optical data input for that. We will calculate these true optical data using parameters $\left\{n^j_0 = 1\ \text{cm}^{-3}, \text{r}^{\text{j}}_{\text{med}}, \sigma^{\text{j}}, \text{m}^{\text{j}}_{\text{R}}, \text{m}^{\text{j}}_{\text{I}}\right\}$ from Table 4. This table contains eight count median radii r_{med} and six geometric standard deviations σ. The effective radius in each case is less than 2.5 μm. This value is significantly higher than the upper end of effective radii that are expected for particles in the fine mode fraction of ambient PSDs [20]. The CRIs range between 1.4 and 1.7 for four chosen real parts [20]. We selected 15 imaginary parts of the CRI in the range from 0 to 0.05 [20]. The overall number of evaluating optical data sets from these input parameters is equal to $8 \cdot 6 \cdot 4 \cdot 15 = 2880$.

For each of these evaluating true optical data $j = 1 \ldots 2880$, we can find two corresponding LUT entries that minimize the discrepancies $\rho^j_{3\beta+2\alpha}$ [see Eq. (16)] and $\rho^j_{2\beta+1\alpha+1\varsigma}$ [see Eq. (22)]. We will limit our consideration by only the CRI of these single LUT elements. The CRIs estimated in such a simple manner can be compared with the true ones.

Figures 5–6 show the statistical distribution of precision that was obtained for the "$2\beta+1\alpha+1\varsigma$" and "$3\beta + 2\alpha$" instrument configurations. The left vertical axis of each plot refers to the number of cases (the total number was 2880 optical data sets) that were tested. The histograms display the statistical distribution of errors of the

retrieved real and imaginary parts of the CRIs. The right vertical axis of each plot refers to the cumulative probability distribution. The cumulative probabilities are shown for both positive and negative retrieval errors. The left and right axes on the plots are scaled to each other. The maximum value of 61% shown on the right axis ("Cumulative probability, %") corresponds to the value of 1750 shown on the left axis ("Number of cases"). Positive values of the horizontal axes mean that the retrieval results overestimated the true values. Negative values show that the retrieval results underestimated the true values. The horizontal axis of Fig. 5 is indexed in increments of 0.05. We chose the step-size of 0.05 because our goal is to achieve a precision of 0.05 for the retrieved real part of the CRI. The horizontal axis of Fig. 6 is incremented in steps of 0.005, which we target regarding the retrieval precision of the imaginary part.

Without providing much further numerical details it is obvious that in this quick test the "$2\beta+1\alpha+1\varsigma$" instrument configuration partially outperformed the "$3\beta+2\alpha$" configuration. The imaginary part for the "$2\beta+1\alpha+1\varsigma$" is surprisingly more often estimated better than 0.005 compared to the "$3\beta+2\alpha$" [see the enhanced central peak with smaller side lobes in Fig. 6]. Unfortunately, the real part on average is getting retrieved with bigger errors in the "$2\beta+1\alpha+1\varsigma$" case [see Fig. 5]. This result can be explained by a smaller number of used input optical data, and fits into our previous studies [15]. Even though the mutual usage of the backscatter and extinction inputs together with just one extra scattering (or absorption, or single-scattering albedo) optical coefficient would significantly improve the inverse retrievals for any lidar configuration.

We would like to stress that the technique used for this noiseless test is not appropriate for the distorted or real data and can be used for the quick look purposes only. Otherwise, the central peak on the retrieval histograms might become undistinguishable.

3. PSD thresholding at 50 nm

During the development of our arrange and average algorithm [15], we were trying to identify the mechanisms of influence of the input parameters on the quality of outputs. As a part of our efforts, the non-uniqueness of the inverse solution is proven to be the major issue because a very different combinations of CRIs and PSDs are able to reproduce the true optical data [see Table 1]. One possible way to get the improvements in the retrievals is to apply some physically meaningful constraints.

As mentioned in Section 2.B, we are mostly concentrated on the accumulation mode aerosols because of their longer lifetime compared to the Aitken mode. At the same time, a separate study by our group employs the LUT from the first version of the arrange and average algorithm to characterize the information content and measurement sensitivities of the "$3\beta+2\alpha$" system. That study shows a specific aspect of the non-uniqueness issue when the retrieval of microphysical parameters in the accumulation mode can be highly affected by Aitken mode solutions that are physically incorrect [22]. The identical interference between the aerosol size modes was noticed during the data processing for the Lindenberg Aerosol Characterization Experiment (LACE 98) [23]. The proposed physical explanation to this effect could be that the used laser wavelength (355 nm at minimum) is not sensitive enough for the observation of such small particles (50 nm radius at maximum). One of the consequences of mismatches between the wavelength and aerosols size is the lack of small scale details on the "$3\beta+2\alpha$" number kernel functions for the radii below 100 nm even for different CRIs [see Fig. 1]. Another consequence is that the different Aitken mode measurement states, i. e., combinations of CRI and PSD, are easily reproducing similar optical coefficients [see Table 1]. Following the recommendation for avoiding this interference [22], the Aitken mode PSDs have to be excluded from the LUT. For instance, the LUT used for the first version of the arrange and average algorithm contains 155,584 entries out of 755,040 to-

tal with PSDs that have more than 30% of their area below 50 nm. Thus, we reduced the number of the LUT entries from 755,040 to 599,456 by the count of the Aitken mode PSDs. We then ran the arrange and average algorithm using the same set of 2880 "$3\beta + 2\alpha$" noiseless evaluating optical data [see Table 4], without changing anything else in our algorithm [15]. Recall that the arrange and average algorithm is based on the property that after total number concentration normalization the simulated/measured optical data can be compared with the LUT. After normalization, all the entries of the LUT are sifted for the multiple times through the procedure of arranging the normalized distances and rejecting those with worse agreement with the measurements. For each run of procedure, only one entry of the LUT can penetrate through that sieve and become an averaging candidate. Outliers are possible, but statistically they are suppressed since the best solutions are counted multiple times during the final averaging.

The comparison of results generated with full (white stars) and reduced (corresponding black stars) LUTs is provided on Fig. 7, one block per microphysical parameter. The left vertical axis of each plot refers to the retrieval error, whereas the right axis helps us to estimate the difference [see Fig. 7; solid curve] between the corresponding reduced [see Fig. 7; ⋆] and full [see Fig. 7; ⋆] LUTs retrieval errors. On the horizontal axis we show the portion of the PSD area below 50 nm. The higher numbers indicate an increase in domination of the Aitken over the accumulation mode aerosols within the PSD. The evaluating optical data set consists of 48 PSDs and 60 CRIs [see Table 4]. Each star in Fig. 7 corresponds to one PSD and 60 CRIs, and shows the averaged value of certain microphysical parameters. Twelve out of 48 PSDs have more than 30% of their areas below 50 nm. The retrieval errors of all microphysical parameters for these twelve PSDs on average became bigger after the LUT reduction [see Fig. 7; the value of the black star almost always exceeds the corresponding white star if the horizontal axis position is above 30%]. It is understandable because the reduced LUT does not cover the Aitken mode as well as before. For the remaining 36 PSDs with less than 30% of Aitken particles in them, the retrieval errors on average became smaller. The improvements are especially noticeable for the total number concentration [see Fig. 7, third block from bottom], which is a very encouraging result because this parameter is always one the most difficult to be retrieved. All other microphysical parameters on average also got better estimations [see Fig. 7, solid curves are staying mostly in the negative domain]. Even the smallest relative retrieval errors for the total surface area concentration on average became slightly smaller [see Fig. 7, second block from bottom].

The 30% threshold mentioned above is not the final number, and is used to provide an example. We are less interested in Aitken mode compared to accumulation mode aerosols, but we still want to have retrievals for particles with radii below 50 nm. The balance should be kept. The unknown factor here is the share of the Aitken mode in ambient PSDs. Real measurements statistics is needed to make a decision about the threshold. In our future studies we plan to perform a comparison between the microphysical parameters retrieved from the lidar measurements and *in situ* data in order to find the balanced Aitken mode threshold.

4. Elements of Error Analysis

Our numerical simulations [7–11, 15] have been continuously surprising by always showing on average the smallest relative retrieval error for the total surface area concentration if at least one extinction optical coefficient was used in the inversion. The representative statistics are available for our arrange and average algorithm [15]. For some previously unknown reason the quality of surface area concentration estimation was almost always better compared to any other microphysical size parameter (e. g., 2% precision for 68.2% of noiseless "$3\beta + 2\alpha$" cases [15]). The effective radius normally was taking second place (e. g., 10% precision for 68.2% of noiseless "$3\beta + 2\alpha$" cases [15]). The total volume concentration usually was in the third position (e. g., 12% precision for 68.2% of noiseless "$3\beta + 2\alpha$"

cases [15]), but not significantly worse than the effective radius. The total number concentration almost always has the largest retrieval error among the four analyzed microphysical size parameters (e. g., 22% precision for 68.2% of noiseless "$3\beta + 2\alpha$" cases [15]).

Going beyond the numerical simulations, we noticed something very similar for retrievals from real data measured by NASA LaRC "$3\beta + 2\alpha$" High Spectral Resolution Lidar (HSRL-2) [2, 3]. HSRL-2 results based on the surface area concentration normally look much smoother and consistent compared to any other microphysical product. The earlier determination of stratospheric aerosol microphysical properties from measurements with a Raman lidar indicated the same feature [24].

In order to explain this stable pattern, let us analyze the behavior of error bars for the total number, surface area, and volume concentrations, and effective radius. To start, we will consider a general case and express the errors of these microphysical size parameters via the errors Δn_0, $\Delta r_{\rm med}$, and $\Delta\sigma$ of the PSD variables n_0, $r_{\rm med}$, and σ correspondingly [25].

Using Eq. (10), the error bar for the total number concentration can be expressed as:

$$\Delta n_{\rm t} = \left|\frac{{\rm d}n_{\rm t}}{{\rm d}n_0}\right| \Delta n_0 = n_{\rm t}\frac{\Delta n_0}{n_0}. \qquad (27)$$

Based on the Eq. (8), we estimate the absolute error for the total surface area concentration as:

$$\Delta s_{\rm t} \approx \left|\frac{\partial s_{\rm t}}{\partial n_0}\right| \Delta n_0 + \left|\frac{\partial s_{\rm t}}{\partial r_{\rm med}}\right| \Delta r_{\rm med} + \left|\frac{\partial s_{\rm t}}{\partial \sigma}\right| \Delta\sigma = \\ = s_{\rm t}\left(\frac{\Delta n_0}{n_0} + 2\frac{\Delta r_{\rm med}}{r_{\rm med}} + 4\ln\sigma\frac{\Delta\sigma}{\sigma}\right). \qquad (28)$$

Equation (11) allows us to present the absolute error for the total volume concentration as:

$$\Delta v_{\rm t} \approx \left|\frac{\partial v_{\rm t}}{\partial n_0}\right| \Delta n_0 + \left|\frac{\partial v_{\rm t}}{\partial r_{\rm med}}\right| \Delta r_{\rm med} + \left|\frac{\partial v_{\rm t}}{\partial \sigma}\right| \Delta\sigma = \\ = v_{\rm t}\left(\frac{\Delta n_0}{n_0} + 3\frac{\Delta r_{\rm med}}{r_{\rm med}} + 9\ln\sigma\frac{\Delta\sigma}{\sigma}\right). \qquad (29)$$

Using Eqs. (27)–(29) we can connect the relative errors of the microphysical size parameters with the relative errors for the PSD variables n_0, $r_{\rm med}$, and σ as:

$$\frac{\Delta n_{\rm t}}{n_{\rm t}} = \frac{\Delta n_0}{n_0}, \qquad (30)$$

$$\frac{\Delta s_{\rm t}}{s_{\rm t}} \approx \frac{\Delta n_0}{n_0} + 2\frac{\Delta r_{\rm med}}{r_{\rm med}} + 4\ln\sigma\frac{\Delta\sigma}{\sigma}, \qquad (31)$$

$$\frac{\Delta v_{\rm t}}{v_{\rm t}} \approx \frac{\Delta n_0}{n_0} + 3\frac{\Delta r_{\rm med}}{r_{\rm med}} + 9\ln\sigma\frac{\Delta\sigma}{\sigma}. \qquad (32)$$

Equations (31)–(32) to a certain degree are able to explain the findings from earlier studies [5–15], that the error of the total surface area concentration is consistently less than the error of the total volume concentration. Our analytical explanation is that for the same set of relative errors $\left\{\frac{\Delta n_0}{n_0}, \frac{\Delta r_{\rm med}}{r_{\rm med}}, \frac{\Delta\sigma}{\sigma}\right\}$, the expression of relative error for the surface area concentration has smaller multiplicative coefficients, i. e., $\{1, 2, 4\}$ [see Eq. (31)]. The coefficients for the volume concentration are noticeably larger, i. e., $\{1, 3, 9\}$ [see Eq. (32)].

The disadvantage of the error bars estimation given by the Eqs. (30)–(32) is obvious. Equation (30) makes one to think that the total number concentration has the smallest retrieval error among the microphysical size parameters. According to our experience [7–11, 15], the situation is exactly opposite. The total number concentration is the most difficult to retrieve with good precision.

The larger errors in the total number concentration from actual retrievals are due to a feature that is not reflected in the theoretical treatment above. While Eqs. (30)–(32) are derived for an arbitrary set of errors $\{\Delta n_0, \Delta r_{\rm med}, \Delta\sigma\}$, the real retrievals include averages of solutions with small discrepancies that are defined in a way similar to Eq. (16).

In order to bring the error bars estimation scheme closer to reality, we have to narrow down the choice of the errors $\left\{\Delta n_0^j, \Delta r_{\rm med}^j, \Delta\sigma^j\right\}$ of the corresponding PSD variables and discover a specific mathematical feature of the considered inverse problem. Let us accept only the combinations $\left\{\tilde{n}_0^j, \tilde{r}_{\rm med}^j, \tilde{\sigma}^j, \tilde{m}_{\rm R}^j, \tilde{m}_{\rm I}^j\right\}$ that minimize the discrepancy $\rho_{3\beta+2\alpha}^j$ [see Eq. (16)]. It is easier to

use the LUT to search for these kind of combinations. We are making this constraining assumption because the small value of similarly defined discrepancies is the main quantitative criteria used by inversion algorithms [5–15]. We will calculate the true values of optical data using parameters $\left\{n_0^j = 1\ \mathrm{cm}^{-3}, \mathrm{r}_{\mathrm{med}}^{\mathrm{j}}, \sigma^{\mathrm{j}}, \mathrm{m}_{\mathrm{R}}^{\mathrm{j}}, \mathrm{m}_{\mathrm{I}}^{\mathrm{j}}\right\}$ from Table 4. Thus, we will get $j = 1 \ldots 2880$ pairs of true PSD variables $\left\{n_0^j, r_{\mathrm{med}}^j, \sigma^j\right\}$ and their corresponding approximations $\left\{\tilde{n}_0^j, \tilde{r}_{\mathrm{med}}^j, \tilde{\sigma}^j\right\}$ originating from the LUT. Since the solutions that satisfy the discrepancy criteria in general differ in their values of total number, surface area, and volume concentrations, the found approximation $\left\{\tilde{n}_0^j, \tilde{r}_{\mathrm{med}}^j, \tilde{\sigma}^j, \tilde{m}_{\mathrm{R}}^j, \tilde{m}_{\mathrm{I}}^j\right\}$ will in general differ from the true solution $\left\{n_0^j, r_{\mathrm{med}}^j, \sigma^j, m_{\mathrm{R}}^j, m_{\mathrm{I}}^j\right\}$.

Let us find the minimum of the difference $\Delta F(\mathrm{k})$ between the true monomodal logarithmic-normal PSDs $f^j(r)$ and their corresponding estimations $\tilde{f}^j(r)$ defined as:

$$\Delta F(\mathrm{k}) = \left\langle \left| \frac{\int_0^\infty r^{\mathrm{k}} \tilde{f}^j(r)\,\mathrm{d}r}{\int_0^\infty r^{\mathrm{k}} f^j(r)\,\mathrm{d}r} - 1 \right| \right\rangle \xrightarrow{\mathrm{k}} \min, \quad (33)$$

where the brackets $|\cdot|$ mean the absolute value and $\langle\cdot\rangle$ designates the averaging among 2880 pairs of available PSD variables. There is some value of degree k for which this difference is minimized. The search is conducted in real values.

Using Eq. (12) we can rewrite Eq. (33) as:

$$\Delta F(\mathrm{k}) = \left\langle \left| \frac{\tilde{n}_0}{n_0} \left(\frac{\tilde{r}_{\mathrm{med}}}{r_{\mathrm{med}}}\right)^{\mathrm{k}} \exp\left(\frac{\mathrm{k}^2\left(\ln^2\tilde{\sigma} - \ln^2\sigma\right)}{2}\right) - 1 \right| \right\rangle \xrightarrow{\mathrm{k}} \min. \quad (34)$$

For the 2880 evaluating optical data sets, the minimum in Eq. (34) is achieved at $\mathrm{k}_{\min} = 1.908$ [see Fig. 8]. This value has important practical meaning because it is very close to the value of degree $\mathrm{k}_{s_t} = 2$ [see Eq. (3)] of the surface area concentration. This finding is another way of looking at the results already seen in Fig. 3. The surface area concentration is relatively constant over the whole range of solutions that reproduce the measurements to within the specified discrepancy threshold, and therefore this microphysical size parameter statistically is retrieved with relatively small uncertainty despite the non-uniqueness of the solution.

Out of the approximate coincidence $\mathrm{k}_{\min} \approx \mathrm{k}_{s_t}$, we can make a theoretical conclusion that statistically the surface area concentration will have the smallest retrieval error compared to the total number [$\mathrm{k}_{n_t} = 0$, see Eq. (2)] and volume [$\mathrm{k}_{v_t} = 3$, see Eq. (4)] concentrations [see Fig. 8 for these points]. That triggers us to express the remaining microphysical size parameters via surface area concentration in order to have a comparison of their retrieval errors with the smallest one. The total number and volume concentrations can be presented as:

$$n_{\mathrm{t}} = \frac{s_{\mathrm{t}}}{4\pi r_{\mathrm{med}}^2 \exp\left(2\ln^2\sigma\right)}, \quad (35)$$

$$v_{\mathrm{t}} = \frac{1}{3} s_{\mathrm{t}} r_{\mathrm{med}} \exp\left(2.5\ln^2\sigma\right). \quad (36)$$

Equations (27) and (29) are transformed into:

$$\Delta n_{\mathrm{t}} \approx \left|\frac{\partial n_{\mathrm{t}}}{\partial s_{\mathrm{t}}}\right| \Delta s_{\mathrm{t}} + \left|\frac{\partial n_{\mathrm{t}}}{\partial r_{\mathrm{med}}}\right| \Delta r_{\mathrm{med}} + \left|\frac{\partial n_{\mathrm{t}}}{\partial \sigma}\right| \Delta\sigma = n_{\mathrm{t}} \left(\frac{\Delta s_{\mathrm{t}}}{s_{\mathrm{t}}} + 2\frac{\Delta r_{\mathrm{med}}}{r_{\mathrm{med}}} + 4\ln\sigma\frac{\Delta\sigma}{\sigma}\right), \quad (37)$$

$$\Delta v_{\mathrm{t}} \approx \left|\frac{\partial v_{\mathrm{t}}}{\partial s_{\mathrm{t}}}\right| \Delta s_{\mathrm{t}} + \left|\frac{\partial v_{\mathrm{t}}}{\partial r_{\mathrm{med}}}\right| \Delta r_{\mathrm{med}} + \left|\frac{\partial v_{\mathrm{t}}}{\partial \sigma}\right| \Delta\sigma = v_{\mathrm{t}} \left(\frac{\Delta s_{\mathrm{t}}}{s_{\mathrm{t}}} + \frac{\Delta r_{\mathrm{med}}}{r_{\mathrm{med}}} + 5\ln\sigma\frac{\Delta\sigma}{\sigma}\right). \quad (38)$$

The absolute error for the effective radius can be estimated using Eq. (9):

$$\Delta r_{\mathrm{eff}} \approx \left|\frac{\partial r_{\mathrm{eff}}}{\partial r_{\mathrm{med}}}\right| \Delta r_{\mathrm{med}} + \left|\frac{\partial r_{\mathrm{eff}}}{\partial \sigma}\right| \Delta\sigma = r_{\mathrm{eff}} \left(\frac{\Delta r_{\mathrm{med}}}{r_{\mathrm{med}}} + 5\ln\sigma\frac{\Delta\sigma}{\sigma}\right). \quad (39)$$

Finally, if discrepancy $\rho_{3\beta+2\alpha}$ is small then estimations given by Eqs. (30) and (32) can be rewritten using the surface area concentration relative error $\frac{\Delta s_{\mathrm{t}}}{s_{\mathrm{t}}}$ as:

$$\frac{\Delta n_{\mathrm{t}}}{n_{\mathrm{t}}} \approx \frac{\Delta s_{\mathrm{t}}}{s_{\mathrm{t}}} + 2\frac{\Delta r_{\mathrm{med}}}{r_{\mathrm{med}}} + 4\ln\sigma\frac{\Delta\sigma}{\sigma}, \quad (40)$$

$$\frac{\Delta v_{\mathrm{t}}}{v_{\mathrm{t}}} \approx \frac{\Delta s_{\mathrm{t}}}{s_{\mathrm{t}}} + \frac{\Delta r_{\mathrm{med}}}{r_{\mathrm{med}}} + 5\ln\sigma\frac{\Delta\sigma}{\sigma}. \quad (41)$$

Equation (39) results in:

$$\frac{\Delta r_{\mathrm{eff}}}{r_{\mathrm{eff}}} \approx \frac{\Delta r_{\mathrm{med}}}{r_{\mathrm{med}}} + 5\ln\sigma\frac{\Delta\sigma}{\sigma} \approx \frac{\Delta v_{\mathrm{t}}}{v_{\mathrm{t}}} - \frac{\Delta s_{\mathrm{t}}}{s_{\mathrm{t}}}. \quad (42)$$

The additives $\frac{\Delta s_t}{s_t}$, $\frac{\Delta r_{med}}{r_{med}}$, and $\frac{\Delta \sigma}{\sigma}$ have noticeably different significance for Eqs. (40)–(42). Previously we already found that under certain assumptions the component $\frac{\Delta s_t}{s_t}$ statistically is fairly small because the degree k_{s_t} = 2 is very close to bring the minimum in the Eq. (33). The geometric standard deviation σ in our study varies from 1.5 to 2.5 [see Table 4]. For the worse-case scenario, the impact $\ln\sigma \frac{\Delta\sigma}{\sigma}$ of its relative error can reach 0.37 (37%). The most significant influence on the error bars has the $\frac{\Delta r_{med}}{r_{med}}$ component because the range of used count median radii r_{med} stretches from 20 to 300 nm [see Table 4]. That causes its relative error to achieve hundreds or even thousands of percents. The influence of the $\frac{\Delta r_{med}}{r_{med}}$ ingredient on the error bar is doubled for the total number concentration compared to the volume one. We claim this to be the reason why the total number concentration is statistically retrieved worse than other considered microphysical size parameters. Compared to the others, $\frac{\Delta n_t}{n_t}$ is twice as much affected by the potentially large error of estimation of the count median radius. Normally we do not retrieve r_{med} explicitly but the existing inversion schemes can theoretically be re-viewed in that way if necessary [5–15]. The absence of the term $\frac{\Delta s_t}{s_t}$ in Eq. (42) perfectly explains why the effective radius is normally retrieved slightly better than total volume but significantly worse than surface area concentration. The missing single component $\frac{\Delta s_t}{s_t}$ is definitely much smaller than $\frac{\Delta r_{med}}{r_{med}} + 5\ln\sigma \frac{\Delta\sigma}{\sigma}$.

On the one side, the Eqs. (40)–(42) were obtained under an assumption that we use the monomodal logarithmic-normal PSD, but the same derivations can be done for the case of multimodality, separately for each mode. On the other side, the results of the real "$3\beta + 2\alpha$" HSRL-2 data processing by Tikhonov's inversion algorithm nicely confirm the theoretical estimations given by these equations [2, 3]. Although the inversion with Tikhonov's regularization does not make any assumption about the shape of the PSD [9–11], it is commonly believed that atmospheric aerosols can be reasonably well approximated by multimodal logarithmic-normal PSDs [18,19]. So it is not surprising that the error behavior derived here using this common assumption is also consistent with the findings from Tikhonov retrievals.

We expect that the other research groups who are developing inversion algorithms for the microphysical parameters retrieval using "$3\beta + 2\alpha$" lidar data are also experiencing similar trends in their results for the total number, surface area, and volume concentrations, and effective radius [6, 9, 13, 14]. In any case, the estimations like Eqs. (40)–(42) theoretically can be derived for PSDs that are different from monomodal logarithmic-normal shape.

5. Analysis of Extinction Number Kernel Functions

In Section 4 we ascertained the fact that the total surface area concentration on average can be retrieved with exceptionally good precision if there is at least one extinction optical coefficient participate in the inversion. Unfortunately, the mechanism that explains why it happens still remains unclear. We only used this numerically confirmed property for our error analysis.

We were trying to find some reasonable explanation in terms of equations or other theoretical derivations and "discovered" an interesting feature of the extinction coefficient that earlier was noticed at least for sulfuric acid aerosols [24]. Other important findings are discussed in separate publication [26], but here we would like to pay special attention to our finding that the averaged extinction number kernel function can be fairly well approximated by simple polynomials as a function of radius. It makes the extinction optical coefficient itself able to provide real-time fast estimation of the correct order of magnitude for some microphysical size parameters.

We started with averaging of the 60 extinction number kernel functions separately at 355 and 532 nm, and used 4 real and 15 imaginary parts of the CRI from Table 4. Figure 9 shows the results. For comparison purposes, we also demonstrate the kernel functions corresponding to the CRI of "Option A.1" input parameters [see Table 1]. The averaged extinction kernel functions for 355 and 532 nm are very similar and can be

well approximated by parabolas. These parabolas are not shown in Fig. 9 because one barely will be able to distinguish the difference between them and averaged curves. Some imperfections on the averaged curves are still visible but they would become much less pronounced if the upper bound of radius range of Fig. 9 would be increased, e. g., from 2.5 to 50 μm.

The oscillations are very noticeable for the extinction number kernel functions corresponding to the "Option A.1" inputs [see Table 1 and Fig. 9]. With an increase of imaginary part of the CRI these oscillations will become much smoother making quadratic approximation more appropriate.

We are interested in decreasing the upper bound of radius range from 2.5 to 0.5 μm because the majority of our 48 targeted PSDs listed in the Table 4 noticeably exceed zero only for the radii from about 0 to 0.5 μm. On a smaller scale the non-parabolic imperfections become more visible but quadratic ($a_{\lambda,2}r^2$) and even cubic ($a_{\lambda,3}r^3$) approximations still fit acceptably well [see Fig. 10]. These approximations have practical meaning because they explain why the extinction optical coefficients are almost linearly proportional to the total surface area and volume concentrations.

Substituting $a_{\lambda,2}r^2$ and $a_{\lambda,3}r^3$ into Eq. (1) instead of extinction kernel function $K_\alpha(m,r,\lambda,p)$ and considering Eqs. (3)–(4), we come up with:

$$\alpha_{355} \approx \int_0^\infty a_{355,2}r^2 f(r)\,\mathrm{d}r = \frac{a_{355,2}}{4\pi}s_\mathrm{t}, \quad (43)$$

$$\alpha_{355} \approx \int_0^\infty a_{355,3}r^3 f(r)\,\mathrm{d}r = \frac{3a_{355,3}}{4\pi}v_\mathrm{t}, \quad (44)$$

$$\alpha_{532} \approx \int_0^\infty a_{532,2}r^2 f(r)\,\mathrm{d}r = \frac{a_{532,2}}{4\pi}s_\mathrm{t}, \quad (45)$$

$$\alpha_{532} \approx \int_0^\infty a_{532,3}r^3 f(r)\,\mathrm{d}r = \frac{3a_{532,3}}{4\pi}v_\mathrm{t}. \quad (46)$$

The total surface area and volume concentrations can be expressed from Eqs. (43)–(46) as:

$$s_\mathrm{t} \approx 4\pi\frac{\alpha_{355}}{a_{355,2}} \approx 4\pi\frac{\alpha_{532}}{a_{532,2}}, \quad (47)$$

$$v_\mathrm{t} \approx \frac{4\pi}{3}\frac{\alpha_{355}}{a_{355,3}} \approx \frac{4\pi}{3}\frac{\alpha_{532}}{a_{532,3}}, \quad (48)$$

where $a_{355,2} = 8.1\ \frac{\mathrm{cm}^3}{\mu\mathrm{m}^2\mathrm{Mm}}$, $a_{355,3} = 18.5\ \frac{\mathrm{cm}^3}{\mu\mathrm{m}^3\mathrm{Mm}}$, $a_{532,2} = 9.8\ \frac{\mathrm{cm}^3}{\mu\mathrm{m}^2\mathrm{Mm}}$, and $a_{532,3} = 22.4\ \frac{\mathrm{cm}^3}{\mu\mathrm{m}^3\mathrm{Mm}}$. These four coefficients are relevant for the 48 PSDs given in Table 4. They should be re-estimated if the range of PSDs is much different from the range [0; 0.5] μm considered here.

We found that the estimation $4\pi\frac{\alpha_{355}}{a_{355,2}}$ works better for the total surface area and $\frac{4\pi}{3}\frac{\alpha_{532}}{a_{532,3}}$ for volume concentrations. The effective radius also can be derived with the help of Eq. (5) as:

$$r_\mathrm{eff} = \frac{3v_\mathrm{t}}{s_\mathrm{t}} \approx \frac{a_{355,2}}{a_{532,3}}\frac{\alpha_{532}}{\alpha_{355}}. \quad (49)$$

For the calculation of effective radius we explicitly used independent estimations of the total surface area and volume concentrations. The absolute error for the effective radius in that case should be derived using Eq. (5) as:

$$\Delta r_\mathrm{eff} \approx \left|\frac{\partial r_\mathrm{eff}}{\partial v_\mathrm{t}}\right|\Delta v_\mathrm{t} + \left|\frac{\partial r_\mathrm{eff}}{\partial s_\mathrm{t}}\right|\Delta s_\mathrm{t} = r_\mathrm{eff}\left(\frac{\Delta v_\mathrm{t}}{v_\mathrm{t}} + \frac{\Delta s_\mathrm{t}}{s_\mathrm{t}}\right). \quad (50)$$

Equation (50) results in:

$$\frac{\Delta r_\mathrm{eff}}{r_\mathrm{eff}} \approx \frac{\Delta v_\mathrm{t}}{v_\mathrm{t}} + \frac{\Delta s_\mathrm{t}}{s_\mathrm{t}}. \quad (51)$$

Comparing Eqs. (42) and (51), one can see that different approaches in estimation of effective radius have different quality. If one is going through the direct retrieval of PSD parameters (e. g., count median radius r_med and geometric standard deviation σ), then effective radius statistically will be estimated slightly better than total volume concentration [see Eq. (42)]. If one is using the scheme that provides independent estimations separately for the surface area and volume concentrations, then their errors will accumulate [see Eq. (51)]. Statistically, it will result in a larger relative error for the effective radius compare to the volume concentration one.

Let us provide a numerical example for the derivations given above. We will use the targeted 2880 noiseless optical data sets from Table 4. Figure 11 shows the results of estimation of surface area and volume concentrations, and

effective radii, one block per parameter. The left and right vertical axes have the same meaning as in Figs. 5–6. The difference is only in scaling. In contrast to Figs. 5–6 we show the results in terms of relative error. The stepsize for the horizontal axis is 10%. We consider 10% relative precision to be an ambitious goal for any algorithm that is used for the retrieval of microphysical size parameters.

The surface area concentration is retrieved in this experiment with average error 16.1%. It has a distinguishable central peak on the histogram [see Fig. 11, top block]. The majority of the cases were estimated with precision better than 20%. We evaluate it to be an impressive result given the easiness of Eq. (47).

Performance of Eqs.(48)–(49) being used for the volume concentration and effective radius estimation is much less accurate. More than 70% of simulated cases are underestimated [see Fig. 11, middle and bottom blocks]. The average error for the volume concentration is 43.9% and for the effective radius is 57.2%. That result nicely confirms our prediction given by Eq. (51). Less than 30% of the considered cases were estimated with precision better than 20%, but the simplicity of the method allows us to use it for the real-time mode quick looks.

Figure 12 provides more details about the results shown by Fig. 11. The total surface area and volume concentrations on average are retrieved with a relative error within 1% smaller for the evaluating cases with higher imaginary parts of the CRI that supports our earlier statement about the appropriateness of the quadratic approximation of the extinction number kernel functions. The averaged relative errors for these two microphysical size parameters have almost identical qualitative behavior, and because of that we demonstrate only one curve which can be used for both parameters [see Fig. 12]. The averaging was done among the 192 evaluating optical data sets for each of 15 imaginary parts of the CRI [see Table 4].

Figures 9–10 and Eq. (47) can serve as an explanation why the total surface area concentration statistically is retrieved with smaller error compared to any other microphysical size parameter. We explicitly used this numerically validated property for our theoretical derivations in Section 4. In fact, the direct measurement of the extinction optical coefficient can be reinterpreted as the straight assessment of the surface area concentration. If the extinction is reproduced by any inversion algorithm with little discrepancy, then surface area on average has proportionally little chance of being wrong. This statement works stronger for the larger particles or bigger imaginary parts of the CRI. The backscatter coefficients which are employed in the inversion also contain the information about PSD and that amplifies the effect.

6. Conclusion

We demonstrated several fundamental aspects of the mathematical problem that has to be solved during retrievals of microphysical parameters from multiwavelength lidar. The most important aspect is that the inverse solution is not unique. If more backscatter and extinction optical coefficients are used as input, then the situation improves in terms of retrievals quality, but even the advanced "$3\beta + 2\alpha$" lidar configuration is not always enough to have one and only one solution. We claim this feature to be the main issue independent of the type or name of the used inversion algorithm. It is not appropriate to consider the inverse problem to be underdetermined only because the algorithm is trying to retrieve more microphysical parameters than there are input data. In provided examples the number of independent unknowns is the same as the number of measurements. The number of the reported microphysical parameters is larger but they are not independent. It is also important to realize that non-uniqueness is a more fundamental problem than instability. A retrieval is called unstable if the inversion produces a large increase in the error, but as this study shows, the retrieval error can be large even with no measurement noise. Realistically, the inverse solution is very close to be non-unique and under certain circumstances the combinations of different CRIs and PSDs result in almost the same "$3\beta + 2\alpha$" optical coefficients.

The theoretically possible way to make the inversion get closer to be the well posed mathematically is to apply constrains of a different kind. For instance, one can start using three different types of input optical data. The backscatter and extinction are already common for such kinds of retrievals. The extra single-scattering albedo, or absorption/scattering coefficient, at least at one extinction wavelength would significantly relax the complexity of the considered problem. We provided an example that the use of a smaller number of "three types" of optical coefficients results in better imaginary part estimations compared to larger number of "two types". The employment of a LUT with fine steps in CRIs and PSDs allows us to take a quick look at possible advantages of different instrument configurations. That LUT itself can be considered as a powerful constraint. The predefined shape of PSDs forces the whole inversion scheme to stay in the area of preferred options. In the current study the monomodal logarithmic-normal shape was used. For the real retrievals we are going to expand the LUT toward the PSD bimodality, as it seems to be a more realistic assumption; however, adding these additional PSDs could increase the non-uniqueness effect in the inversion. Therefore, we must carefully investigate the best way to expand the LUT to better reflect bimodal distributions in the atmosphere and address the non-uniqueness in the retrieval.

We confirmed a retrieval interference between the Aitken and accumulation mode aerosols that is especially noticeable for the total number concentration. By limiting the participation of the Aitken mode, we improved the performance of our arrange and average algorithm for cases where the accumulation mode was dominant. We expect that the other inversion algorithms are also affected by this effect.

We offered our explanation of the statistical behavior of microphysical size parameters in the case of "$3\beta + 2\alpha$" lidar configuration. We found that the almost ideal parabolic behavior of the extinction number kernel function and the logarithmic-normal shape of the PSDs caused the total surface area concentration to have the smallest and the total number concentration to have the largest retrieval errors. The analytical expression for the total surface area concentration can be considered as the correlation law between the PSD variables of optical data sets that are non-uniquely reproducing the true one. These results are valid both for the inversion of simulated and real data by different algorithms.

We noticed another firm correlation: between the extinction optical coefficients and total surface area concentration. It explains why this particular microphysical size parameter is retrieved with smaller error than the others in the case of "$3\beta + 2\alpha$" lidar configuration. We found that the correlation is getting stronger with increase of imaginary part of the CRI that slightly improves the retrieval of the total surface area concentration. This effect is quite weak but we still expect it to be observable in all existing inversion schemes.

We are very grateful to James W. Closs for the wording and grammar support.

References

1. T. F. Stocker, D. Qin, G.-K. Plattner, M. Tignor, S. K. Allen, J. Boschung, A. Nauels, Y. Xia, V. Bex and, P. M. Midgley, eds., *IPCC. Climate Change 2013. The Physical Science Basis. Contribution of Working Group I to the Fifth Assessment Report of the Intergovernmental Panel on Climate Change* (Cambridge University, 2013).
2. D. Müller, C. A. Hostetler, R. A. Ferrare, S. P. Burton, E. Chemyakin, A. Kolgotin, J. W. Hair, A. L. Cook, D. B. Harper, R. R. Rogers, R. W. Hare, C. S. Cleckner, M. D. Obland, J. Tomlinson, L. K. Berg, and B. Schmid, "Airborne Multiwavelength High Spectral Resolution Lidar (HSRL-2) observations during TCAP 2012: vertical profiles of optical and microphysical properties of a smoke/urban haze plume over the northeastern coast of the US," Atmos. Meas. Tech. **7**, 3487–3496 (2014).
3. P. Sawamura, R. H. Moore, S. P. Burton, E. Chemyakin, D. Müller, A. Kolgotin, R. A. Ferrare, C. A. Hostetler, L. D. Ziemba, and A. J. Beyersdorf, "Evaluation of HSRL-2

aerosol microphysical retrievals: comparison to in-situ measurements during DISCOVER-AQ 2013," (in preparation).

4. A. N. Tikhonov and V. Y. Arsenin, eds., *Solution of Ill-Posed Problems* (Wiley, 1977).
5. D. P. Donovan and A. I. Carswell, "Principle component analysis applied to multiwavelength lidar aerosol backscatter and extinction measurements," Appl. Opt. **36**, 9406–9424 (1997).
6. M. de Graaf, A. Apituley, and D. P. Donovan, "Feasibility study of integral property retrieval for tropospheric aerosol from Raman lidar data using principal component analysis," Appl. Opt. **52**, 2173–2186 (2013).
7. D. Müller, U. Wandinger, and A. Ansmann, "Microphysical particle parameters from extinction and backscatter lidar data by inversion with regularization: theory," Appl. Opt. **38**, 2346–2357 (1999).
8. D. Müller, U. Wandinger, and A. Ansmann, "Microphysical particle parameters from extinction and backscatter lidar data by inversion with regularization: simulation," Appl. Opt. **38**, 2358–2368 (1999).
9. I. Veselovskii, A. Kolgotin, V. Griaznov, D. Müller, U. Wandinger, and D. N. Whiteman, "Inversion with regularization for the retrieval of tropospheric aerosol parameters from multiwavelength lidar sounding," Appl. Opt. **41**, 3685–3699 (2002).
10. I. Veselovskii, A. Kolgotin, V. Griaznov, D. Müller, K. Franke, and D. N. Whiteman, "Inversion of multiwavelength Raman lidar data for retrieval of bimodal aerosol size distribution," Appl. Opt. **43**, 1180–1195 (2004).
11. A. Kolgotin and D. Müller, "Theory of inversion with two-dimensional regularization: profiles of microphysical particle properties derived from multiwavelength lidar measurements," Appl. Opt. **47**, 4472–4490 (2008).
12. C. Böckmann, "Hybrid regularization method for the ill-posed inversion of multiwavelength lidar data in the retrieval of aerosol size distributions," Appl. Opt. **40**, 1329–1342 (2001).
13. C. Böckmann, I. Miranova, D. Müller, L. Scheidenbach, and R. Nessler, "Microphysical aerosol parameters from multiwavelength lidar," J. Opt. Soc. Am. A **22**, 518–528 (2005).
14. I. Veselovskii, O. Dubovik, A. Kolgotin, M. Korenskiy, D. N. Whiteman, K. Allakhverdiev, and F. Huseyinoglu, "Linear estimation of particle bulk parameters from multi-wavelength lidar measurements," Atmos. Meas. Tech. **5**, 1135–1145 (2012).
15. E. Chemyakin, D. Müller, S. Burton, A. Kolgotin, C. Hostetler, and R. Ferrare, "Arrange and average algorithm for the retrieval of aerosol parameters from multiwavelength high-spectral-resolution lidar/Raman lidar data," Appl. Opt. **53**, 7252–7266 (2014).
16. A. Kolgotin, D. Müller, E. Chemyakin, and A. Romanov, "Perspectives of the explicit retrieval of the complex refractive index of aerosols from optical data taken with lidar," Proceedings of ILRC 27, July 2015, New York, PS-B5-17.
17. C. F. Bohren and D. R. Huffman, eds., *Absorption and Scattering of Light by Small Particles* (Wiley, 1983).
18. W. C. Hinds, ed., *Aerosol Technology. Properties, Behavior and Measurement of Airborne Particles* (Wiley, 1999).
19. J. H. Seinfeld and S. N. Pandis, eds., *Atmospheric Chemistry and Physics. From Air Pollution to Climate Change* (Wiley, 2006).
20. O. Dubovik, B. Holben, T. F. Eck, A. Smirnov, Y. J. Kaufman, M. D. King, D. Tanré, and I. Slutsker, "Variability of absorption and optical properties of key aerosol types observed in worldwide locations," J. Atmos. Sci. **59**, 590–608 (2002).
21. J. W. Hair, C. A. Hostetler, A. L. Cook, D. B. Harper, R. A. Ferrare, T. L. Mack, W. Welch, L. R. Izquierdo, and F. E. Hovis, "Airborne High Spectral Resolution Lidar for profiling aerosol optical properties," Appl. Opt. **47**, 6734–6752 (2008).
22. S. P. Burton et al., "Information content and sensitivity of the "$3\beta + 2\alpha$" lidar measurement system for microphysical retrievals," (in preparation).
23. U. Wandinger, D. Müller, C. Böckmann, D. Althausen, V. Matthias, J. Bösenberg, V. Weiß, M. Fiebig, M. Wendisch, A. Stohl, and A. Ansmann, "Optical and microphysical characterization of biomass-burning and industrial-pollution aerosols from multiwavelength lidar and aircraft measurements," J. Geophys. Res. **107(D21)**, 8125, 10.129/2000JD000202

(2002).
24. U. Wandinger, A. Ansmann, J. Reichardt, and T. Deshler, "Determination of stratospheric aerosol microphysical properties from independent extinction and backscattering measurements with a Raman lidar," Appl. Opt. **34**, 8315–8329 (1995).
25. J. R. Taylor, ed., *An Introduction to Error Analysis. The Study of Uncertainties in Physical Measurements* (University Science Books, 1997).
26. A. Kolgotin, D. Müller, E. Chemyakin, and A. Romanov, "Inversion of profiles of lidar optical data: gradient correlation method for improved constrainment of the solution space of aerosol microphysical properties, part 1: theory," (in preparation).

List of Figure Captions

Fig. 1. "$3\beta + 2\alpha$" number kernel functions and two groups ("A" and "B") each consisting of three bell shaped PSDs for the input parameters given in Tables 1–2. The solid line is used to represent both "Reference" columns, whereas dashed and dotted lines depict "Option 1" and "Option 2". f01.eps.

Fig. 2. 56,170 sets of total surface area concentration s_{t} and effective radius r_{eff} that are employed in the LUT. f02.eps.

Fig. 3. Distribution of the effective radius r_{eff}, unitless coefficient $n_{3\beta+2\alpha}$, and corrected total surface area $\hat{s}_{\mathrm{t}}$ and volume concentrations $\hat{v}_{\mathrm{t}}$ on the CRI plane for the entries of the LUT subset $\left\{\mathrm{LUT}^{0.3\%}_{3\beta+2\alpha}\right\}$. The corresponding true "Reference A" values [see Table 1] are separately shown in the right bottom corner of each block. Radius of every bubble qualitatively represents the parameter value. f03.eps.

Fig. 4. Spatial distribution of the CRIs for the LUT subsets $\left\{\mathrm{LUT}^{0.3\%}_{3\beta}\right\}$ (top left), $\left\{\mathrm{LUT}^{0.3\%}_{2\beta+1\alpha}\right\}$ (top right), $\left\{\mathrm{LUT}^{0.3\%}_{3\beta+1\alpha}\right\}$ (bottom left), and $\left\{\mathrm{LUT}^{0.3\%}_{2\beta+1\alpha+1\varsigma}\right\}$ (bottom right). The pentagon symbol shows the position of the "Reference A" CRI [see Table 1]. f04.eps.

Fig. 5. Noiseless retrieval of the real part of the CRI for the "$2\beta + 1\alpha + 1\varsigma$" instrument configuration (solid line) and the "$3\beta + 2\alpha$" lidar configuration (dashed line). Negative values indicate underestimation in the retrievals whereas positive values mean overestimation. f05.eps.

Fig. 6. Noiseless retrieval of the imaginary part of the CRI. The notation is the same as in Fig. 5. f06.eps.

Fig. 7. Influence of the Aitken mode on the accumulation mode particles retrieval. White stars depict the performance of the arrange and average algorithm with full LUT. Black stars refer to the results with reduced LUT. Solid curve shows the difference between the reduced LUT ($\star$) and full LUT ($\star$) retrievals using the axis on the right hand side. Dashed line borders the 30% threshold. Variable names are the same as in Table 1. f07.eps.

Fig. 8. Minimization of the weighted difference between the true and estimated PSDs. f08.eps.

Fig. 9. Averaged and "Option A.1" [see Table 1] extinction number kernel functions. f09.eps.

Fig. 10. Quadratic and cubic approximations of the averaged extinction number kernel function. f10.eps.

Fig. 11. Noiseless retrieval of the total surface area and volume concentrations, and effective radius, using only two extinction optical coefficients. f11.eps.

Fig. 12. Averaged relative error for noiseless retrieval of the total surface area (s_{t}) and volume (v_{t}) concentrations. f12.eps.

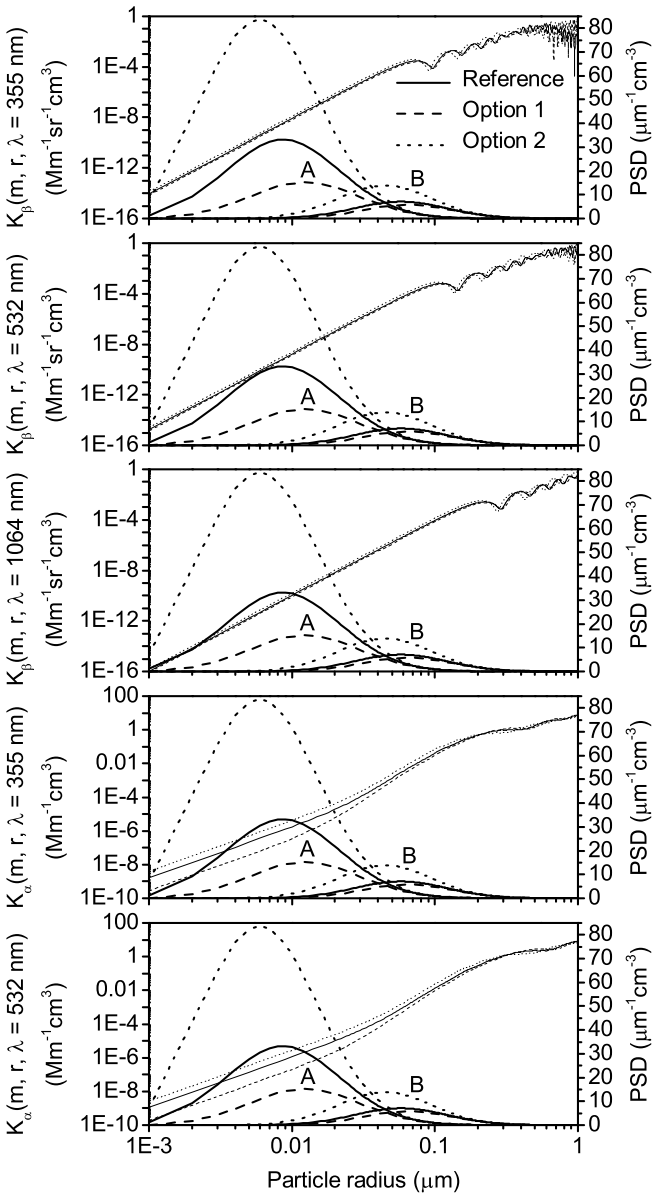

Fig. 1. "$3\beta + 2\alpha$" number kernel functions and two groups ("A" and "B") each consisting of three bell shaped PSDs for the input parameters given in Tables 1–2. The solid line is used to represent both "Reference" columns, whereas dashed and dotted lines depict "Option 1" and "Option 2". f01.eps.

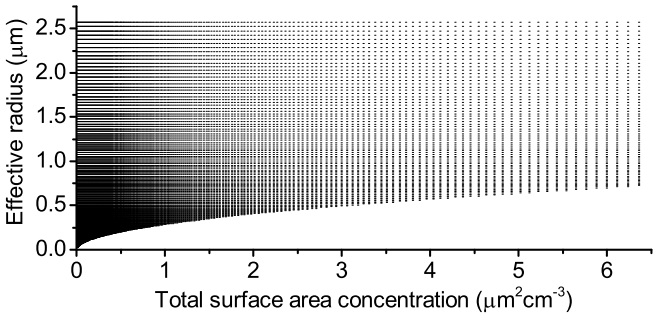

Fig. 2. 56,170 sets of total surface area concentration s_{t} and effective radius r_{eff} that are employed in the LUT. f02.eps.

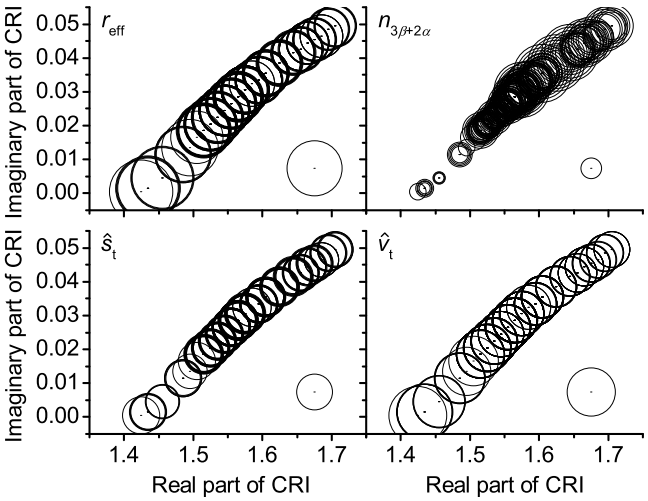

Fig. 3. Distribution of the effective radius r_{eff}, unitless coefficient $n_{3\beta+2\alpha}$, and corrected total surface area $\hat{s}_t$ and volume concentrations $\hat{v}_t$ on the CRI plane for the entries of the LUT subset $\left\{\text{LUT}^{0.3\%}_{3\beta+2\alpha}\right\}$. The corresponding true "Reference A" values [see Table 1] are separately shown in the right bottom corner of each block. Radius of every bubble qualitatively represents the parameter value. f03.eps.

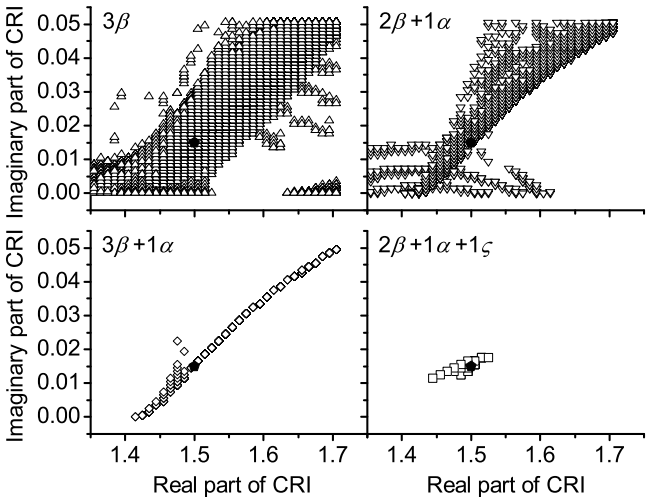

Fig. 4. Spatial distribution of the CRIs for the LUT subsets $\left\{\text{LUT}^{0.3\%}_{3\beta}\right\}$ (top left), $\left\{\text{LUT}^{0.3\%}_{2\beta+1\alpha}\right\}$ (top right), $\left\{\text{LUT}^{0.3\%}_{3\beta+1\alpha}\right\}$ (bottom left), and $\left\{\text{LUT}^{0.3\%}_{2\beta+1\alpha+1\varsigma}\right\}$ (bottom right). The pentagon symbol shows the position of the "Reference A" CRI [see Table 1]. f04.eps.

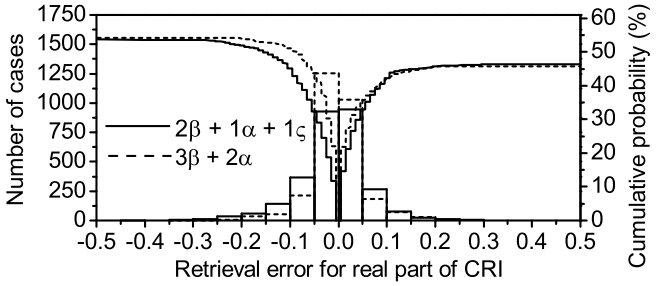

Fig. 5. Noiseless retrieval of the real part of the CRI for the "$2\beta + 1\alpha + 1\varsigma$" instrument configuration (solid line) and the "$3\beta + 2\alpha$" lidar configuration (dashed line). Negative values indicate underestimation in the retrievals whereas positive values mean overestimation. f05.eps.

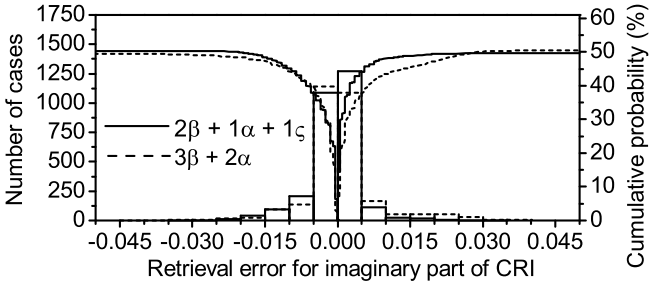

Fig. 6. Noiseless retrieval of the imaginary part of the CRI. The notation is the same as in Fig. 5. f06.eps.

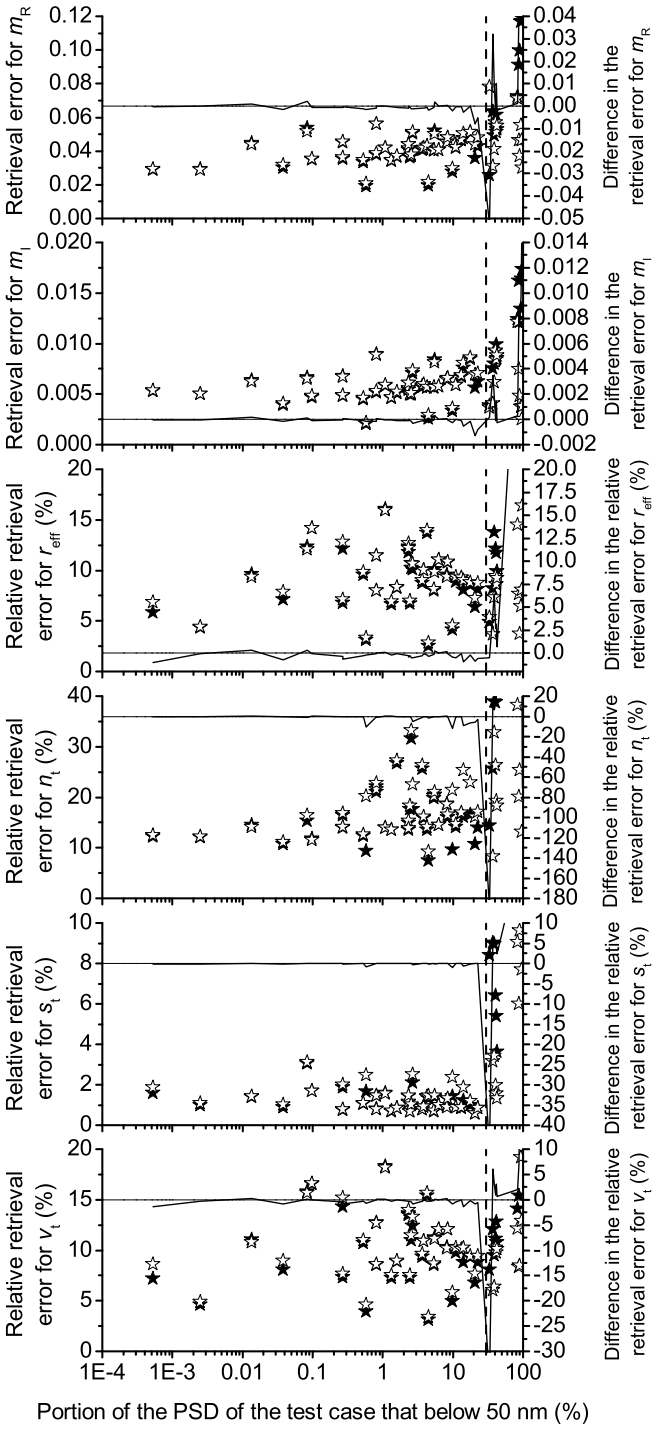

Fig. 7. Influence of the Aitken mode on the accumulation mode particles retrieval. White stars depict the performance of the arrange and average algorithm with full LUT. Black stars refer to the results with reduced LUT. Solid curve shows the difference between the reduced LUT (⋆) and full LUT (✰) retrievals using the axis on the right hand side. Dashed line borders the 30% threshold. Variable names are the same as in Table 1. f07.eps.

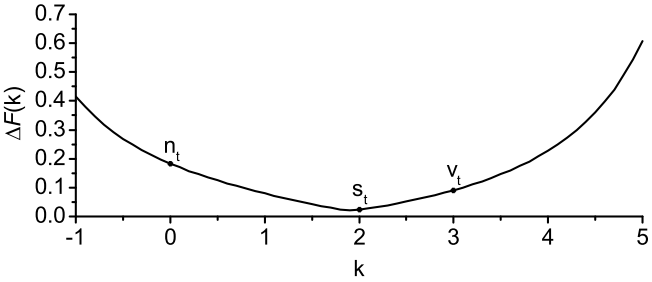

Fig. 8. Minimization of the weighted difference between the true and estimated PSDs. f08.eps.

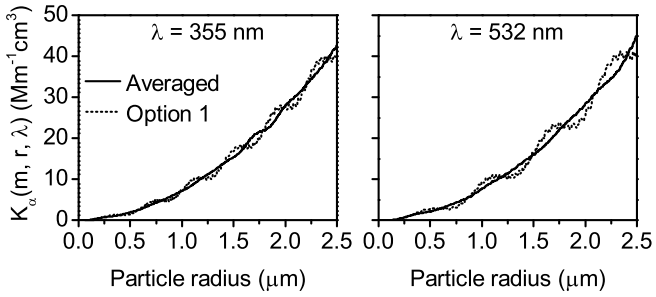

Fig. 9. Averaged and "Option A.1" [see Table 1] extinction number kernel functions. f09.eps.

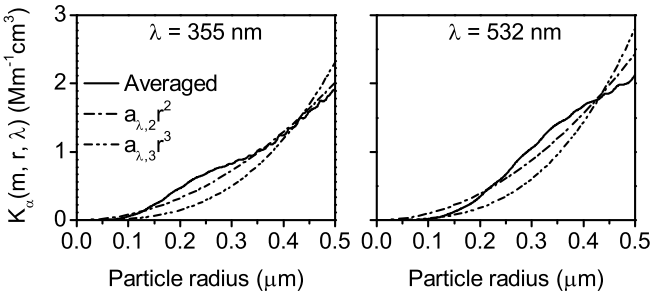

Fig. 10. Quadratic and cubic approximations of the averaged extinction number kernel function. f10.eps.

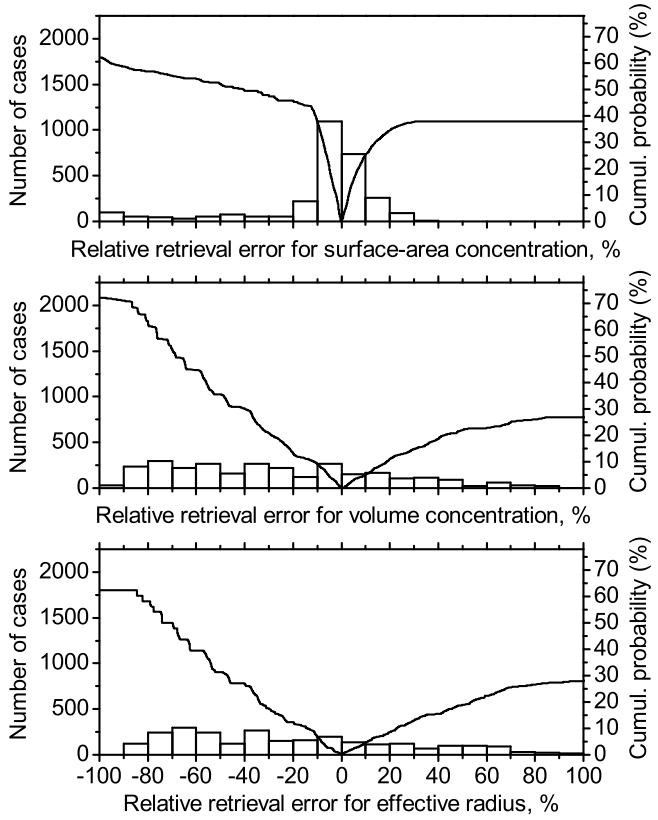

Fig. 11. Noiseless retrieval of the total surface area and volume concentrations, and effective radius, using only two extinction optical coefficients. f11.eps.

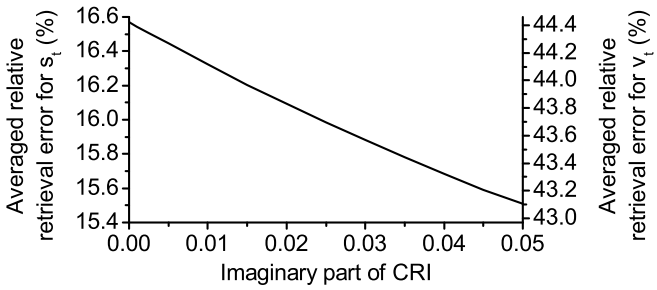

Fig. 12. Averaged relative error for noiseless retrieval of the total surface area (s_t) and volume (v_t) concentrations. f12.eps.

Table 1. The reference and two optional sets of Aitken mode input parameters resulting in very similar "$3\beta + 2\alpha$" optical coefficients[a]

Parameter	Reference A	Option A.1	Option A.2
$n_0\left(\frac{1}{\mathrm{cm}^3}\right)$	1	0.609846	1.81519
$r_{\mathrm{med}}\,(\mu\mathrm{m})$	0.02	0.026722	0.0143
σ	2.5	2.41493	2.56124
m_{R}	1.5	1.44262	1.63858
m_{I}	0.015	0.00249	0.040493
$\beta_{355}\left(\frac{1}{\mathrm{Mm\ sr}}\right)$	$2.297{\cdot}10^{-4}$	$2.297{\cdot}10^{-4}$	$2.296{\cdot}10^{-4}$
$\Delta\beta_{355}$ (%)	0	−0.01832	−0.076349
$\beta_{532}\left(\frac{1}{\mathrm{Mm\ sr}}\right)$	$1.500{\cdot}10^{-4}$	$1.499{\cdot}10^{-4}$	$1.502{\cdot}10^{-4}$
$\Delta\beta_{532}$ (%)	0	−0.068815	0.097481
$\beta_{1064}\left(\frac{1}{\mathrm{Mm\ sr}}\right)$	$6.285{\cdot}10^{-5}$	$6.284{\cdot}10^{-5}$	$6.283{\cdot}10^{-5}$
$\Delta\beta_{1064}$ (%)	0	−0.019134	−0.031577
$\alpha_{355}\left(\frac{1}{\mathrm{Mm}}\right)$	$1.136{\cdot}10^{-2}$	$1.137{\cdot}10^{-2}$	$1.135{\cdot}10^{-2}$
$\Delta\alpha_{355}$ (%)	0	0.088928	−0.00803
$\alpha_{532}\left(\frac{1}{\mathrm{Mm}}\right)$	$7.993{\cdot}10^{-3}$	$7.994{\cdot}10^{-3}$	$7.994{\cdot}10^{-3}$
$\Delta\alpha_{532}$ (%)	0	0.017477	0.018641
ω_{355}	0.898016	0.979015	0.800886
$\Delta\omega_{355}$ (%)	0	9.01981	−10.8161
ω_{532}	0.904254	0.981022	0.807858
$\Delta\omega_{532}$ (%)	0	8.48972	−10.6602
ω_{1064}	0.896946	0.979821	0.792656
$\Delta\omega_{1064}$ (%)	0	9.23976	−11.6272
$n_{\mathrm{t}}\left(\frac{1}{\mathrm{cm}^3}\right)$	1	0.609846	1.81519
Δn_{t} (%)	0	−39.0154	81.5188
$s_{\mathrm{t}}\left(\frac{\mu\mathrm{m}^2}{\mathrm{cm}^3}\right)$	0.026948	0.042476	0.015072
Δs_{t} (%)	0	57.6225	−44.0687
$v_{\mathrm{t}}\left(\frac{\mu\mathrm{m}^3}{\mathrm{cm}^3}\right)$	0.001466	0.002642	0.000656
Δv_{t} (%)	0	80.2515	−55.2537
$r_{\mathrm{eff}}\,(\mu\mathrm{m})$	0.163156	0.186579	0.130528
Δr_{eff} (%)	0	14.3564	−19.9978

[a]The term n_0 means the parameter of proportion, r_{med} is the count median radius, and σ is the geometric standard deviation. CRI real (m_{R}) and imaginary (m_{I}) parts are kept particle size and wavelength independent. The backscatter coefficients (β) and single-scattering albedo (ω) are calculated at wavelengths 355, 532, and 1064 nm. The extinction coefficients (α) are given at wavelength 355 and 532 nm. The total number (n_{t}), surface area (s_{t}), and volume (v_{t}) concentrations, and effective radius (r_{eff}) are also provided for the comparison. This can be done using corresponding Δ-lines that are offered in percentages as compared with the reference value for each computed parameter.

Table 2. The reference and two optional sets of accumulation mode input parameters resulting in very similar "$3\beta + 2\alpha$" optical coefficients[a]

Parameter	Reference B	Option B.1	Option B.2
$n_0\left(\frac{1}{\mathrm{cm}^3}\right)$	1	0.877246	1.55255
$r_{\mathrm{med}}\,(\mu\mathrm{m})$	0.1	0.108699	0.078682
σ	2.1	2.07204	2.1213
m_{R}	1.5	1.47207	1.63939
m_{I}	0.015	0.008033	0.040766
$\beta_{355}\left(\frac{1}{\mathrm{Mm\ sr}}\right)$	$6.992{\cdot}10^{-3}$	$6.993{\cdot}10^{-3}$	$6.987{\cdot}10^{-3}$
$\Delta\beta_{355}$ (%)	0	0.01515	−0.082439
$\beta_{532}\left(\frac{1}{\mathrm{Mm\ sr}}\right)$	$5.515{\cdot}10^{-3}$	$5.51{\cdot}10^{-3}$	$5.52{\cdot}10^{-3}$
$\Delta\beta_{532}$ (%)	0	−0.088615	0.078643
$\beta_{1064}\left(\frac{1}{\mathrm{Mm\ sr}}\right)$	$2.696{\cdot}10^{-3}$	$2.699{\cdot}10^{-3}$	$2.695{\cdot}10^{-3}$
$\Delta\beta_{1064}$ (%)	0	0.0845849	−0.044588
$\alpha_{355}\left(\frac{1}{\mathrm{Mm}}\right)$	$2.55{\cdot}10^{-1}$	$2.55{\cdot}10^{-1}$	$2.551{\cdot}10^{-1}$
$\Delta\alpha_{355}$ (%)	0	0.0109398	0.052241
$\alpha_{532}\left(\frac{1}{\mathrm{Mm}}\right)$	$2.381{\cdot}10^{-1}$	$2.381{\cdot}10^{-1}$	$2.381{\cdot}10^{-1}$
$\Delta\alpha_{532}$ (%)	0	−0.021901	−0.003679
ω_{355}	0.857338	0.911602	0.746436
$\Delta\omega_{355}$ (%)	0	6.32943	−12.9356
ω_{532}	0.887841	0.933024	0.786016
$\Delta\omega_{532}$ (%)	0	5.08902	−11.4689
ω_{1064}	0.911272	0.948603	0.818949
$\Delta\omega_{1064}$ (%)	0	4.0966	−10.1313
$n_{\mathrm{t}}\left(\frac{1}{\mathrm{cm}^3}\right)$	1	0.877246	1.55255
Δn_{t} (%)	0	−12.2754	55.2549
$s_{\mathrm{t}}\left(\frac{\mu\mathrm{m}^2}{\mathrm{cm}^3}\right)$	0.37787	0.429218	0.241095
Δs_{t} (%)	0	13.5886	−36.1963
$v_{\mathrm{t}}\left(\frac{\mu\mathrm{m}^3}{\mathrm{cm}^3}\right)$	0.049876	0.058621	0.026
Δv_{t} (%)	0	17.5341	−47.8695
$r_{\mathrm{eff}}\,(\mu\mathrm{m})$	0.395974	0.409728	0.323528
Δr_{eff} (%)	0	3.47356	−18.2955

[a]Variable names are the same as in Table 1.

Table 3. Parameters that were used for computing the optical data and microphysical parameters in the look-up table "LUT"[a]

m_{R}	1.295	1.305	1.315	1.325	1.335	1.345	1.355
	and so on up to 1.705						
$m_{\mathrm{I}} \cdot 10^{-3}$	0	0.5	1.5	2.5	3.5	4.5	5.5
	and so on up to 50.5						
$s_{\mathrm{t}}\left(\frac{\mu\mathrm{m}^2}{\mathrm{cm}^3}\right)$	{0.005, 0.0051, 0.005202, 0.00530604,						
	and so on up to $0.005 \cdot 1.02^{361}$}						
$r_{\mathrm{eff}}\,(\mu\mathrm{m})$	{0.025, 0.0255, 0.02601, 0.0265302,						
	and so on up to $0.025 \cdot 1.02^{234}$}						

[a]Variable names are the same as in Table 1.

Table 4. Parameters that were used for computing the evaluating optical data and microphysical parameters.

r_{med} (nm)	20	60	100	140	180	220	260	300
σ	1.5	1.7	1.9	2.1	2.3	2.5		
m_{R}	1.4	1.5	1.6	1.7				
$m_{\mathrm{I}} \cdot 10^{-3}$	0	0.1	1.0	2.5	5.0	7.5	10.0	15.0
	20.0	25.0	30.0	35.0	40.0	45.0	50.0	

[a]Variable names are the same as in Table 1.